

Isogeometric Analysis of Solids in Boundary Representation



Sven Klinkel and Margarita Chasapi

Abstract In this chapter, we present boundary-oriented numerical methods to analyze three-dimensional solid structures. For the analysis, the original geometry of the solid is employed according to the isogeometric paradigm. For the parametrization of the domain, the idea of the scaled boundary finite element method is adopted. Hence, the boundary of the solid is sufficient to describe the entire domain. The presented approaches employ analytical and numerical solution methods such as the Galerkin and collocation methods. To illustrate the applicability in the analysis procedure, three formulations are elaborated and demonstrated by means of numerical examples. The advantages compared to standard numerical methods are discussed thoroughly.

1 Introduction

Typically solids are designed by the boundary representation modeling technique in computer-aided design (CAD) software (Stroud 2006). From the analysis point of view, the finite element method (FEM) is the most popular numerical technique. The geometry and the displacement response of the structure are approximated by Lagrange basis functions. This leads in general to an approximation of the geometry, which accordingly affects the accuracy of deformation results (Cottrell et al. 2009). To circumvent the geometrical approximation error, an exact description from the CAD model could be employed. This is the idea of the isogeometric analysis, which was introduced by Hughes et al. (2005). The main concept is to employ the same NURBS basis functions in order to describe the geometry and to approximate the displacements. However, for three-dimensional solids a three-dimensional tensor-product structure of NURBS objects must be adopted in isogeometric analysis in

The financial support of the German Research Foundation (DFG) under Grant No. KL1345/10-1 is gratefully acknowledged.

S. Klinkel (✉) · M. Chasapi
RWTH Aachen University, Aachen, Germany
e-mail: klinkel@lbb.rwth-aachen.de

© CISM International Centre for Mechanical Sciences 2020
J. Schröder and P. de Mattos Pimenta (eds.), *Novel Finite Element Technologies for Solids and Structures*, CISM International Centre for Mechanical Sciences 597,
https://doi.org/10.1007/978-3-030-33520-5_6

order to parameterize the physical domain (Cottrell et al. 2009; Düster et al. 2008; Temizer et al. 2012; Rank et al. 2012). Such a trivariate tensor–product structure, however, is not defined in the CAD model. In CAD, only the boundary surfaces of the solid are defined. A classical volumetric discretization of the inner domain becomes, therefore, a complicated task. This observation motivated the development of numerical formulations in which the solid is defined by its boundary, and only this boundary is used for isogeometric analysis. These so-called *boundary-oriented solid formulations* combine the advantages of boundary-oriented methods and isogeometric analysis.

Currently, the most well-known boundary-oriented methods are the boundary element method (BEM) and the scaled boundary finite element method (SB-FEM). The latter one is a special kind of fundamental solution-less boundary element method, which was introduced by Song and Wolf (1997, 1998). The basic idea lies on a boundary scaling technique. In the analysis, the solid is defined by its boundary and a scaling center. The scaling center is chosen in a zone from which the total boundary of the solid is visible (Song and Wolf 1997). The scaling center C will, in general, be located inside the domain. A radial scaling parameter ξ is introduced to conduct the scaling process. Hence, $\xi = 1$ represents the boundary of the solid and $\xi = 0$ denotes the scaling center, while $0 < \xi < 1$ describes a certain point inside the domain. Scaling the boundary of the solid with respect to the specified scaling center yields the solid, see Fig. 1. In the analysis, only the tensor–product structure of the boundary is employed, which is different from the “polar mesh” suggested by Bazilevs et al. (2014). In the SB-FEM approach, it is distinguished between parameters in the circumferential direction and in the radial scaling direction. The weak form of equilibrium is only enforced in the circumferential direction. In the scaling direction, the equilibrium is strongly applied. In the framework of linear elasticity, a second-order ordinary differential equation (ODE) is obtained in terms of the scaling parameter. In the circumferential direction a finite element approximation is employed, which utilizes the Lagrange basis functions (Song and Wolf 1997, 1998) or the NURBS basis functions as investigated by Lin et al. (2014), Natarajan et al. (2015),

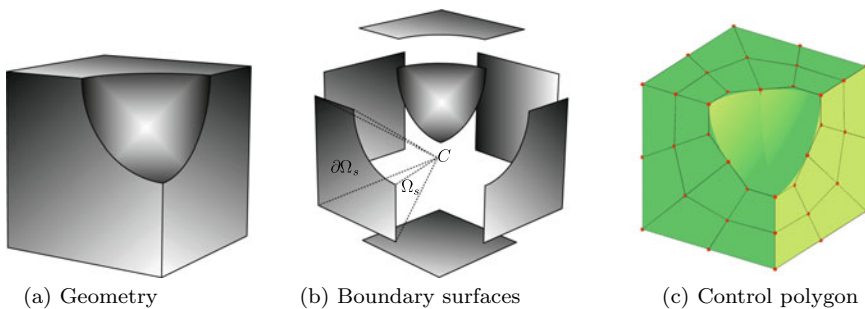


Fig. 1 Geometry and control net of cube with spherical intersection. The geometry is created in CAD with the boundary representation modeling technique

Klinkel et al. (2015), and Chen et al. (2015, 2016) for the description of the geometry and the displacement. The Lagrange basis functions will lead to an approximation of the geometry. For linear elastic problems, the second-order ODE can be solved analytically or numerically. Analytical approaches include the eigenvalue method and the matrix function solution (Song and Wolf 1998). For the eigenvalue method, by introducing a dual vector form of the differential equation, the second-order ODE is reduced to first-order ODE according to Song and Wolf (1998) and Song (2004). Then, the eigenvalue problem of the first-order ODE is solved, which leads to the displacement response of the domain. An extension to nonlinear problems was proposed by Lin and Liao (2011), Ooi et al. (2014) and Behnke et al. (2014). The former one suggested an approach for nonlinear SB-FEM based on the homotopy analysis method. The latter studies are based on nonlinear shape functions derived from the solution of linear problems, which are employed for the nonlinear analysis. Besides the analytical approaches, a NURBS-based collocation approach has been proposed to solve the ODE numerically by Klinkel et al. (2015) for 2D and by Chen et al. (2015) for 3D problems. For this numerical approach, certain approximation is made for the choice of the first collocation point due to the numerical instability arising at the scaling center. Furthermore, a NURBS-based Galerkin approach has been proposed by Chen et al. (2016) to solve elasticity problems of boundary-represented solids. Moreover, Chasapi and Klinkel (2018) proposed the treatment of nonlinear problems by employing the approximation with NURBS and the Galerkin method for the solution in scaling direction.

In this chapter, boundary-oriented numerical methods are presented to solve the elasticity problem of solids in boundary representation. The chapter summarizes the main results of the publications Klinkel et al. (2015), Chen et al. (2015, 2016) and Chasapi and Klinkel (2018). The boundary scaling technique is employed to describe the solid. Thus, the boundary is exactly described in isogeometric analysis. Three numerical approaches will be demonstrated: the semi-analytical method, the NURBS-based hybrid collocation-Galerkin method and the NURBS-based Galerkin method. In the first two approaches, the weak form of equilibrium is enforced in the circumferential direction. The response in radial scaling direction is derived from the eigenvalue method and the collocation method accordingly. In the last approach, the weak form of equilibrium is employed in the radial scaling and circumferential direction. In all cases, NURBS basis functions are employed for the description of the boundary geometry as well as for the approximation of the displacements at the boundary. The displacement response in the radial scaling direction is approximated by one-dimensional NURBS basis functions for the numerical solution. Each approach results in a global system of equations, the solution of which yields the displacement response at the boundary surfaces and in the interior domain.

The outline of the chapter is as follows. In Sect. 2, the parametrization is presented. Section 3 provides the governing equations for linear elasticity of 3D problems. In Sect. 4, methods for the numerical approximation are presented. First, the basics of B-splines and NURBS as interpolation functions are illustrated. Moreover, a semi-analytical approach based on the eigenvalue method in radial scaling direction is given. Here, the derivation of the scaled boundary finite element equation is

addressed. Furthermore, a NURBS-based collocation approach is presented. Here, NURBS basis functions are employed for the approximation, whereas the collocation method yields the solution in radial scaling direction. Finally, a NURBS-based Galerkin approach is presented. Here, the weak form of equilibrium discretized with NURBS is applied in all parametric directions. In Sect. 5, numerical examples are presented to evaluate the accuracy of the numerical methods. Suggestions for the optimum choice of the polynomial degree of collocation NURBS and the number of collocation points are provided. Furthermore, comparisons to the standard FEM and isogeometric analysis are given.

2 Parametrization

In this Section, the basic concept of the transformation of the geometry is provided. The main idea is based on the scaled boundary finite element method as proposed by Song and Wolf (1997, 1998). For the transformation, a radial scaling parameter is introduced to define the geometry of the solid. The boundary of the solid is thus scaled with respect to a scaling center C , see Fig. 2. The coordinates of C are denoted as $\hat{\mathbf{x}}_0$. The scaling center is defined such that the total boundary of the solid is visible (Song and Wolf 1997). The radial scaling parameter ξ runs from the scaling center toward the boundary, where $\xi = 0$ corresponds to the scaling center C and $\xi = 1$ describes the boundary of the solid. The total domain is partitioned into sectional domains $\Omega = \bigcup_{s=1}^{n_{sec}} \Omega_s$. Each sectional domain is parametrized in the circumferential direction to describe the boundary $\partial\Omega_s$.

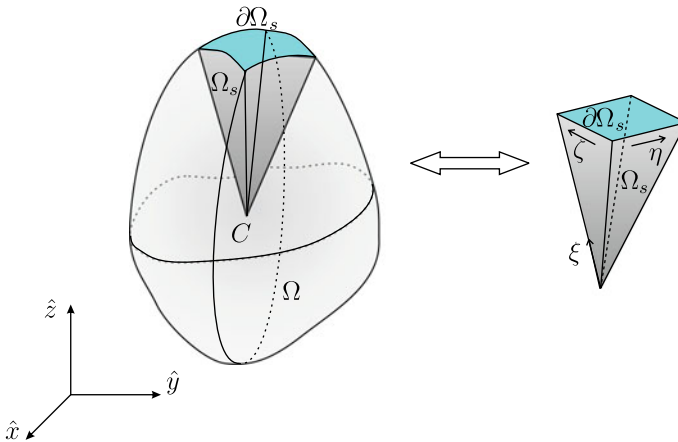


Fig. 2 The three-dimensional domain Ω and the sectional domain Ω_s in the physical space and the parameter space

For 3D problems, the boundary of each sectional domain Ω_s is a surface, see Fig. 2, and parametrized in the circumferential direction with η and ζ . It holds $0 \leq \eta \leq 1$ and $0 \leq \zeta \leq 1$. The scaling center C is defined as $\hat{\mathbf{x}}_0 = (\hat{x}_0, \hat{y}_0, \hat{z}_0)^T$. The position of a point on the boundary surfaces is denoted by $\mathbf{x}_s = (x_s, y_s, z_s)^T$ and a point in the interior of the solid is described by $\hat{\mathbf{x}}_s = (\hat{x}_s, \hat{y}_s, \hat{z}_s)^T$. Let $N_s(\eta, \zeta)$ be a matrix of shape functions employed to describe the boundary surfaces. An arbitrary point on the boundary surfaces or in the domain is given as

$$\mathbf{x}_s = N_s(\eta, \zeta) \mathbf{X} \quad \text{on } \partial\Omega_s, \quad \hat{\mathbf{x}}_s = \hat{\mathbf{x}}_0 + \xi(N_s(\eta, \zeta) \mathbf{X} - \hat{\mathbf{x}}_0) \quad \text{in } \Omega_s. \quad (1)$$

Here, we employ the NURBS basis functions to define the geometry of the boundary surfaces. This conforms ideally to the boundary representation modeling technique used in CAD. The vector \mathbf{X} represents the coordinates of the control points on the boundary. Its dimension is $n_{st} = 3 \cdot n_{bs}$, where n_{bs} is the number of control points on the boundary.

Considering Eq. (1) yields the Jacobian matrix

$$\mathbf{J} = \begin{bmatrix} \frac{\partial \hat{x}_s}{\partial \xi} & \frac{\partial \hat{y}_s}{\partial \xi} & \frac{\partial \hat{z}_s}{\partial \xi} \\ \frac{\partial \hat{x}_s}{\partial \eta} & \frac{\partial \hat{y}_s}{\partial \eta} & \frac{\partial \hat{z}_s}{\partial \eta} \\ \frac{\partial \hat{x}_s}{\partial \zeta} & \frac{\partial \hat{y}_s}{\partial \zeta} & \frac{\partial \hat{z}_s}{\partial \zeta} \end{bmatrix} = \begin{bmatrix} 1 & 0 & 0 \\ 0 & \xi & 0 \\ 0 & 0 & \xi \end{bmatrix} \underbrace{\begin{bmatrix} x_s - \hat{x}_0 & y_s - \hat{y}_0 & z_s - \hat{z}_0 \\ \frac{\partial x_s}{\partial \eta} & \frac{\partial y_s}{\partial \eta} & \frac{\partial z_s}{\partial \eta} \\ \frac{\partial x_s}{\partial \zeta} & \frac{\partial y_s}{\partial \zeta} & \frac{\partial z_s}{\partial \zeta} \end{bmatrix}}_{\bar{\mathbf{J}}} \quad (2)$$

It results in a multiplicative decomposition of the determinant $\det \mathbf{J} = \xi^2 \det \bar{\mathbf{J}} = \xi^2 \bar{J}$. The transformation of a volume element dV from the physical space to the parameter space reads

$$dV = d\hat{x} d\hat{y} d\hat{z} = \hat{\mathbf{x}}_{s,\xi} \cdot (\hat{\mathbf{x}}_{s,\eta} \times \hat{\mathbf{x}}_{s,\zeta}) d\xi d\eta d\zeta = \xi^2 \bar{J} d\xi d\eta d\zeta. \quad (3)$$

3 Governing Equations

The governing equations for the three-dimensional (3D) problem is formulated in the Cartesian coordinates $(\hat{x}, \hat{y}, \hat{z})$, see Fig. 2. The displacement vector is defined as $\mathbf{u} = \mathbf{u}(\hat{x}, \hat{y}, \hat{z}) = [u_{\hat{x}}, u_{\hat{y}}, u_{\hat{z}}]^T$. It is assumed that the 3D domain Ω is bounded by $\partial\Omega = \partial_u\Omega \cup \partial_t\Omega$, where $\partial_u\Omega$ is the boundary with a prescribed displacement $\bar{\mathbf{u}}$ and $\partial_t\Omega$ is the boundary with a prescribed traction $\bar{\mathbf{t}}$. Here, the Neumann boundary condition does not overlap with the Dirichlet boundary condition, that is $\partial_u\Omega \cap \partial_t\Omega = \emptyset$.

The differential equation of motion reads

$$\mathbf{D}\boldsymbol{\sigma} + \rho\mathbf{b} = \mathbf{0} \quad (4)$$

where ρ is the mass density, \mathbf{b} is the body force, and \mathbf{D} is the linear differential operator.

The relation between the strains $\boldsymbol{\varepsilon}$ and the displacements \mathbf{u} is given as

$$\boldsymbol{\varepsilon} = \mathbf{D}^T \mathbf{u}. \quad (5)$$

The stresses and strains are related by the elasticity matrix \mathbb{C}

$$\boldsymbol{\sigma} = \mathbb{C} \boldsymbol{\varepsilon}. \quad (6)$$

The Dirichlet and Neumann boundary conditions read

$$\mathbf{u} = \bar{\mathbf{u}} \quad \text{on } \partial_u \Omega, \quad \mathbf{n} \boldsymbol{\sigma} = \bar{\mathbf{t}} \quad \text{on } \partial_t \Omega. \quad (7)$$

The matrix \mathbf{n} contains the components of the outward unit normal vector. Equations (4)–(7) are the general formulas for elastostatic problems. For the 3D case, the strains are denoted by $\boldsymbol{\varepsilon} = [\varepsilon_x, \varepsilon_y, \varepsilon_z, \gamma_{yz}, \gamma_{xz}, \gamma_{xy}]^T$ and the stresses as $\boldsymbol{\sigma} = [\sigma_x, \sigma_y, \sigma_z, \tau_{yz}, \tau_{xz}, \tau_{xy}]^T$. Let \mathbf{D} be the differential operator

$$\mathbf{D} = \begin{bmatrix} \frac{\partial}{\partial x} & 0 & 0 & 0 & \frac{\partial}{\partial z} & \frac{\partial}{\partial y} \\ 0 & \frac{\partial}{\partial y} & 0 & \frac{\partial}{\partial z} & 0 & \frac{\partial}{\partial x} \\ 0 & 0 & \frac{\partial}{\partial z} & \frac{\partial}{\partial y} & \frac{\partial}{\partial x} & 0 \end{bmatrix}. \quad (8)$$

The elasticity matrix \mathbb{C} is written as

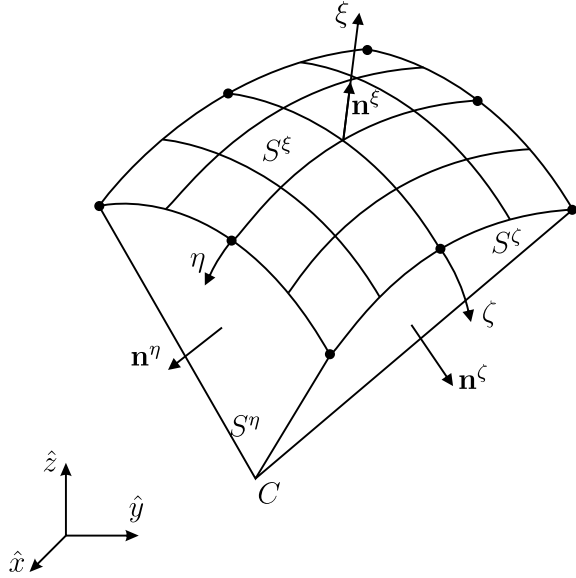
$$\mathbb{C} = \frac{E}{(1+\nu)(1-2\nu)} \begin{bmatrix} 1-\nu & \nu & \nu & 0 & 0 & 0 \\ \nu & 1-\nu & \nu & 0 & 0 & 0 \\ \nu & \nu & 1-\nu & 0 & 0 & 0 \\ 0 & 0 & 0 & \frac{1-\nu}{2} & 0 & 0 \\ 0 & 0 & 0 & 0 & \frac{1-\nu}{2} & 0 \\ 0 & 0 & 0 & 0 & 0 & \frac{1-\nu}{2} \end{bmatrix}. \quad (9)$$

The outward unit normal vector \mathbf{n} is given as

$$\mathbf{n} = \begin{bmatrix} n_{\hat{x}} & 0 & 0 & 0 & n_{\hat{z}} & n_{\hat{y}} \\ 0 & n_{\hat{y}} & 0 & n_{\hat{z}} & 0 & n_{\hat{x}} \\ 0 & 0 & n_{\hat{z}} & n_{\hat{y}} & n_{\hat{x}} & 0 \end{bmatrix} \quad (10)$$

where $n_{\hat{x}}$, $n_{\hat{y}}$, and $n_{\hat{z}}$ are the components of the outward unit normal vector on $\partial\Omega$. Employing the parametrization of Sect. 2, each section is bounded by five surfaces, see Fig. 2. The normal vectors \mathbf{n}^ξ , \mathbf{n}^η , and \mathbf{n}^ζ are perpendicular to the surfaces described by the parameters (η, ζ) , (ζ, ξ) , and (ξ, η) , respectively, see Fig. 3. The formulas for the determination of the outward normal vectors and the description of the infinitesimal surface elements dS^ξ , dS^η , dS^ζ are given in the Appendix.

Fig. 3 The boundary of one 3D sectional domain is partitioned in $\partial\Omega_s = S^\xi \cup S^\eta \cup S^\zeta$



With the help of Eqs. (2), (8), and (A.1)–(A.3), the differential operator \mathbf{D} is rewritten as

$$\mathbf{D} = \frac{1}{J} \left[\mathbf{b}_\xi \frac{\partial}{\partial \xi} + \frac{1}{\xi} \left(\mathbf{b}_\eta \frac{\partial}{\partial \eta} + \mathbf{b}_\zeta \frac{\partial}{\partial \zeta} \right) \right] \tag{11}$$

with the coefficient matrices

$$\mathbf{b}_i^T = g^i \begin{bmatrix} n_x^i & 0 & 0 & 0 & n_z^i & n_y^i \\ 0 & n_y^i & 0 & n_z^i & 0 & n_x^i \\ 0 & 0 & n_z^i & n_y^i & n_x^i & 0 \end{bmatrix} \quad (i = \xi, \eta, \zeta) \tag{12}$$

Using Eq. (12), the traction $\bar{\mathbf{t}} = \mathbf{n}\boldsymbol{\sigma}$ on any of the boundary surfaces (η, ζ) , (ζ, ξ) and (ξ, η) can be rewritten as

$$\bar{\mathbf{t}}^i = \frac{1}{g^i} \mathbf{b}_i^T \boldsymbol{\sigma} \quad (i = \xi, \eta, \zeta) \tag{13}$$

Substituting Eq. (11) into Eqs. (5) and (6), we obtain the strains and stresses in the parameter space. However, it should be noted that there is a denominator in Eq. (11). The strains and stresses will exhibit singularity at the scaling center C , as at this point $\xi = 0$ holds. Here, the singularity does not arise from the method itself, but from the employed parametrization. The singularity will arise in the context of a solution to the strong form of the equation. To obviate the singularity in this case, we choose a tolerance in calculating the strains and stresses at the scaling center, see also Sect.4.3.

4 Numerical Approximation

4.1 Boundary Description

The boundary surfaces of solids are described by nonuniform rational B-Splines (NURBS) in CAD. In the scope of isogeometric analysis, the same functions are employed for the approximation of the solution. In this Section, the basics of B-Splines and NURBS for the boundary description of the 3D domain will be introduced. For better illustration, the functions are first presented for curves (1D) and further extended to surfaces (2D). B-spline curves in the three-dimensional space \mathbb{R}^3 are defined by a set of n control points

$$\mathbf{B}_i = [x_i, y_i, z_i]^T = [\mathbf{X}_i^T]^T \quad i = 1, \dots, n \quad (14)$$

and the open knot vector

$$\Xi = \{\xi_1, \xi_2, \dots, \xi_{n+p+1}\}, \quad (15)$$

where p is the polynomial degree of the B-spline basis functions. The entries ξ_i in the knot vector are nondecreasing. Intervals $[\xi_i, \xi_{i+1}]$ with $i = 1, \dots, n + p$ are referred to as knot spans. The control points \mathbf{B}_i are the nodal values in \mathbb{R}^3 , which define the location in space of the B-spline curve $\mathbf{X}(\xi)$. The piecewise straight connection lines from \mathbf{B}_i to \mathbf{B}_{i+1} for $i = 1$ until $i = n - 1$ form the so-called control polygon, which is a piecewise linear approximation of the curve $\mathbf{X}(\xi)$, see Fig. 4. The B-spline basis functions $N_i^p(\xi)$ are defined recursively by the Cox-de Boor formula

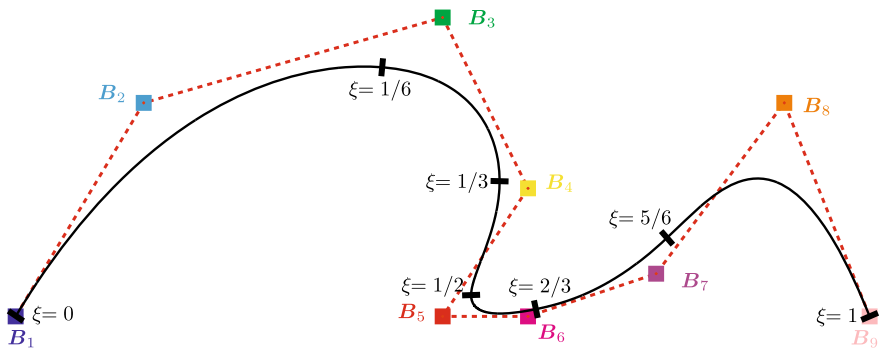


Fig. 4 Physical curve (solid black line) and control polygon (dotted red line) of a B-spline curve of order $p = 3$ with the knot vector $\Xi = \{0, 0, 0, 0, \frac{1}{6}, \frac{1}{3}, \frac{1}{2}, \frac{2}{3}, \frac{5}{6}, 1, 1, 1\}$

$$\begin{aligned}
 p = 0 : \quad N_i^0(\xi) &= \begin{cases} 1 & \text{if } \xi_i \leq \xi \leq \xi_{i+1} \\ 0 & \text{otherwise} \end{cases} \\
 p > 0 : \quad N_i^p(\xi) &= \frac{\xi - \xi_i}{\xi_{i+p} - \xi_i} N_i^{p-1}(\xi) + \frac{\xi_{i+p+1} - \xi}{\xi_{i+p+1} - \xi_{i+1}} N_{i+1}^{p-1}(\xi) .
 \end{aligned}
 \tag{16}$$

The basis functions establish a map from the parameter space defined by the knot vector Ξ to the physical B-spline curve

$$\mathbf{X}(\xi) = \sum_{i=1}^n N_i^p(\xi) \mathbf{B}_i \quad \xi_1 \leq \xi \leq \xi_{n+p+1} .
 \tag{17}$$

The support of basis functions is local and the influence of the control point \mathbf{B}_i is limited to that interval. The number of basis functions which have influence on one knot span is given by $n_{en} = p + 1$. In the interval $[\xi_i, \xi_{i+1}]$, the basis functions N_{i-p}^p to N_i^p are nonzero.

Figure 4, a B-spline curve together with its control polygon is given. The associated basis functions are given in Fig. 5. Hereby each basis function is plotted in the same color as its associated control point. The knot values are denoted by a black stroke. The locally confined influence of the basis functions in each knot interval is clearly visible in Fig. 5. One important property for the usage of B-Splines as interpolation functions is the partition of unity

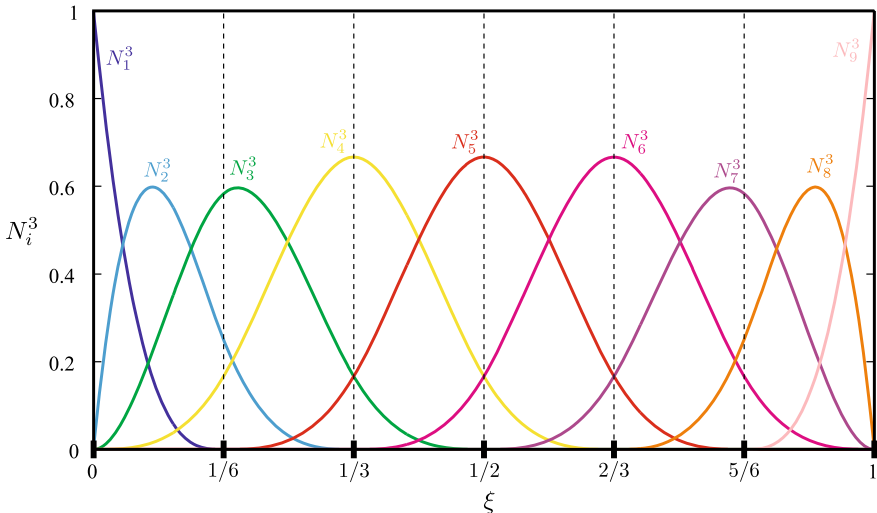


Fig. 5 Basis functions for the B-spline curve displayed in Fig. 4

$$\sum_{i=1}^n N_i^p(\xi) = 1 \quad \forall \xi \in \Xi. \quad (18)$$

Further properties are the affine invariance, non-negativity, and variation diminishing property. A significant advantage of B-splines is that higher continuity allows the computation of $p - m$ continuous derivatives at knots and of an infinite number of derivatives within knot spans. Also, with the rising order of B-splines the smoothness of the curve increases in contrast to higher order Lagrange basis functions, which can entail oscillations. Univariate B-splines can be directly incorporated for the approximation of the solution in the radial scaling direction of the solid, see also Sects. 4.3 and 4.4.

NURBS curves are nonuniform rational B-splines. Their rational character allows an exact description of conic sections, such as circles. They can be understood as a projection of four-dimensional curves projected onto \mathbb{R}^3 (Cottrell et al. 2009). The notion of four dimensions is kept in the definition of the four-dimensional control points

$$\mathbf{B}_i = [x_i, y_i, z_i, w_i]^T = [\mathbf{X}_i^T, w_i]^T \quad i = 1, \dots, n. \quad (19)$$

Together with a knot vector, as given in Eq. (15), they define a NURBS curve of order p . The fourth coordinate w_i is the weight factor of the respective control point. All definitions and properties of B-splines hold accordingly, except the definition of the physical curve and the derivatives thereof. A physical point $\mathbf{X}(\xi)$ on the NURBS curve

$$\mathbf{X}(\xi) = \frac{\sum_{i=1}^n N_i^p(\xi) w_i \mathbf{X}_i}{\sum_{i=1}^n N_i^p(\xi) w_i} \quad \xi_1 \leq \xi \leq \xi_{n+p+1} \quad (20)$$

is computed with the help of the B-spline basis functions $N_i^p(\xi)$ given in Eq. (16) under consideration of the weight factor w_i . The definition of rational basis functions allows the expression of Eq. (20) in a simple form

$$\mathbf{X}(\xi) = \sum_{i=1}^n R_i^p(\xi) \mathbf{X}_i \quad \text{with} \quad R_i^p(\xi) = \frac{N_i^p(\xi) w_i}{\sum_{i=1}^n N_i^p(\xi) w_i}, \quad \xi_1 \leq \xi \leq \xi_{n+p+1} \quad (21)$$

akin to the B-spline case. The weight w_i of a control point \mathbf{B}_i quantifies the influence of this control point in comparison to the other control points. If the weight is increased, the NURBS curve will tend toward this control points. In the limit $w_i \rightarrow 0$, the curve will behave as if the control point is not present. The influence of the weight is limited to the influence interval of the associated control point. Outside this interval, the curve is not affected by an alteration of the weight. By setting the weights to $w_i = 1$ for all control points, the curve is deduced to a B-spline. This approach can be employed for the approximation in the scaling direction, where only straight radial lines are defined (see Sect. 4.3 and 4.4).

Now that we have gathered all necessary expressions to define one-dimensional NURBS, we can easily extend these to the two-dimensional case by employing the parametrization of the solid in Sect. 2. The geometry of the boundary surface $\partial\Omega_s$ is described by a NURBS surface, which is created by a tensor-product combination of the two knot vectors $\mathbf{H} = \{\eta_1, \eta_2, \dots, \eta_{n_\eta+p+1}\}$ and $\mathbf{Z} = \{\zeta_1, \zeta_2, \dots, \zeta_{n_\zeta+q+1}\}$. The orders of the basis functions along each parametric direction η and ζ are denoted by p and q , respectively. The control points \mathbf{B}_{ij} are in general arranged in a rectangular grid called control point net. They are identified by a double index (ij) in parentheses, where the first number $i \in \{1, 2, \dots, n_\eta\}$ denotes the position of the control point in η -direction. Analogously, $j \in \{1, 2, \dots, n_\zeta\}$ identifies the position in ζ -direction.

The four components of the control points

$$\mathbf{B}_{(ij)} = [x_{(ij)}, y_{(ij)}, z_{(ij)}, w_{(ij)}]^T = [\mathbf{X}_{(ij)}^T, w_{(ij)}]^T \tag{22}$$

correspond to the spatial coordinates $\mathbf{X}_{(ij)}$ and the weight factor $w_{(ij)}$. The total number of control points is denoted by $n_{bs} = n_\eta \cdot n_\zeta$. The projection of the control point net from a four-dimensional space \mathbb{R}^4 to a surface embedded in the three-dimensional space \mathbb{R}^3 is carried out with the help of the rational NURBS basis functions $R_{(ij)}^{pq}(\eta, \zeta)$. The univariate B-spline basis functions given in Eq. (16) are used for both parametric directions and multiplied with the weight $w_{(ij)}$ to arrive at the rational NURBS surface basis functions

$$R_{(ij)}^{pq}(\eta, \zeta) = \frac{N_i^p(\eta) N_j^q(\zeta) w_{(ij)}}{\sum_{i=1}^{n_\eta} \sum_{j=1}^{n_\zeta} N_i^p(\eta) N_j^q(\zeta) w_{(ij)}}. \tag{23}$$

In analogy to the univariate B-spline, there are only $n_{en} = (p + 1)(q + 1)$ nonzero basis functions in each knot span that have an impact on the arbitrary rectangle $[\eta_i, \eta_{i+1}] \times [\zeta_j, \zeta_{j+1}]$. The number of potentially nonzero rectangles within a NURBS surface is given by $n_{el} = (n_1 - p_1)(n_2 - p_2)$. For a pair of parameters $(\eta, \zeta) \in [\eta_{i_0}, \eta_{i_0+1}] \times [\zeta_{j_0}, \zeta_{j_0+1}]$ a physical point \mathbf{x}_s on the NURBS surface can be determined by

$$\mathbf{x}_s(\eta, \zeta) = \sum_{i=i_0-p}^{i_0} \sum_{j=j_0-q}^{j_0} R_{(ij)}^{pq}(\eta, \zeta) \mathbf{X}_{(ij)}. \tag{24}$$

Recall that this is the definition of the boundary geometry (see also Eq. 1) and keep in mind that the same definition will be employed for the approximation of the solution at the boundary (see also Eq. 27). All properties mentioned above for B-spline and NURBS curves can be carried forward to NURBS surfaces. The interested reader is referred to the studies of Piegl and Tiller (1997) as well as Cottrell et al. (2009) for more details on B-splines and NURBS.

For 3D problems, following the isogeometric concept, the displacements $\mathbf{u}_s(\xi = 1, \eta, \zeta)$ at the boundary surfaces are approximated with the same basis shape functions as the original geometry of the CAD model. Therefore, it holds

$$\mathbf{x}_s = \sum_{ij=1}^{n_{bs}} R_{(ij)}^{pq}(\eta, \zeta) \mathbf{X}_{(ij)} \quad \mathbf{u}_s = \sum_{ij=1}^{n_{bs}} R_{(ij)}^{pq}(\eta, \zeta) \mathbf{U}_{(ij)}, \quad (25)$$

where $\mathbf{X}_{(ij)}$ defines the coordinate of the control point (ij) and n_{bs} denotes the total number of control points at the boundary surface $\partial\Omega_s$. The nodal displacement degrees of freedom are arranged akin in the vector $\mathbf{U}_{(ij)}$. $R_{(ij)}^{pq}(\eta, \zeta)$ is the NURBS basis function employed to describe the boundary surfaces, which is termed as boundary NURBS. The corresponding control points are denoted as boundary control points.

Considering Eq. (25) and rearranging all control point vectors $\mathbf{U}_{(ij)}$ in the vector \mathbf{U}_s , the approximation of the displacement at the boundary surface reads

$$\mathbf{u}_s = \underbrace{\begin{bmatrix} R_1 & 0 & 0 & R_2 & 0 & 0 & \dots & R_{n_{bs}} & 0 & 0 \\ 0 & R_1 & 0 & 0 & R_2 & 0 & \dots & 0 & R_{n_{bs}} & 0 \\ 0 & 0 & R_1 & 0 & 0 & R_2 & \dots & 0 & 0 & R_{n_{bs}} \end{bmatrix}}_{N_s(\eta, \zeta)} \mathbf{U}_s \quad (26)$$

Note that a bijective mapping holds between the subscript $I = 1, 2, \dots, n_{bs}$ and the control point (ij) . Considering Eqs. (25) and (26), the approximation of the displacements and the virtual displacements on the sectional domain Ω_s are defined as

$$\mathbf{u}(\xi, \eta, \zeta) = N_s(\eta, \zeta) \mathbf{U}_s(\xi), \quad \delta \mathbf{u}(\xi, \eta, \zeta) = N_s(\eta, \zeta) \delta \mathbf{U}_s(\xi), \quad (27)$$

where \mathbf{U}_s contains all nodal degrees of freedom in the circumferential direction of Ω_s . Accordingly, $\delta \mathbf{U}_s$ contains all virtual nodal displacements. An example of the interpolation in the circumferential direction of the boundary is illustrated in Fig. 6 for a 3D problem.

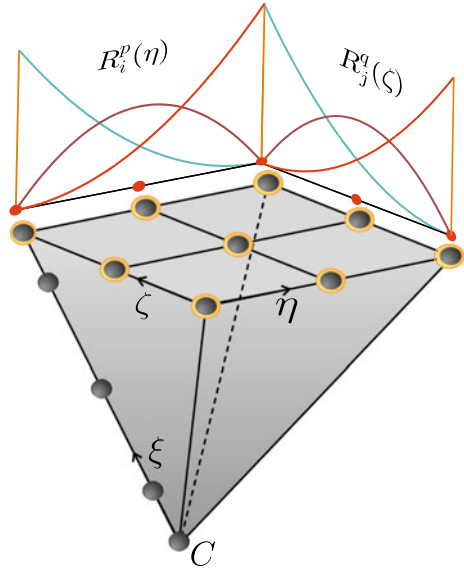
4.2 Scaled Boundary Finite Element Equation

The weak form of equilibrium can be derived by multiplying Eq. (4) with a test function $\delta \mathbf{u}$. Integration over the whole domain, application of integration by parts and consideration of the Neumann boundary condition in Eq. (7) yields the weak form

$$\sum_{s=1}^{nsec} \left(\int_{\Omega_s} \delta \boldsymbol{\varepsilon}^T \boldsymbol{\sigma} \, dV - \int_{\partial\Omega_s} \delta \mathbf{u}^T \bar{\mathbf{t}} \, dS - \int_{\Omega_s} \delta \mathbf{u}^T \boldsymbol{\rho} \mathbf{b} \, dV \right) = \mathbf{0}, \quad (28)$$

where $nsec$ is the total number of sectional domains Ω_s . The first term of Eq. (28) represents the internal virtual work, the second term is the external virtual work done by the boundary tractions, and the third term is the external virtual work done by

Fig. 6 Illustration of NURBS basis functions in the parameter space for 3D problems. The boundary NURBS basis functions $R_i^p(\eta)$ and $R_j^q(\zeta)$ with $p = 2$ and $q = 2$ are shown. $n_{bs} = 3 \times 3$ control points are employed in η and ζ directions



the body forces. The virtual strains are given as $\delta \boldsymbol{\epsilon} = \mathbf{D}^T \delta \mathbf{u}(\xi, \eta, \zeta)$. Note that only the boundary surfaces $\partial \Omega_s$ are approximated with NURBS as described in Sect. 4.1, whereas the solution in the radial scaling direction is carried out analytically. The stress vector is computed by $\boldsymbol{\sigma} = \mathbf{C} \mathbf{D}^T \mathbf{u}$ using Eqs. (5) and (6). The first term in Eq. (28) is rewritten by employing integration by parts to

$$\int_{\Omega_s} \delta \boldsymbol{\epsilon}^T \boldsymbol{\sigma} \, dV = \delta \mathbf{U}_s^T \left(\xi^2 \mathbf{k}_{11} \mathbf{U}_{s,\xi} + \xi \mathbf{k}_{21} \mathbf{U}_s \right) \Big|_{\xi=0}^{\xi=1} - \int_0^1 \delta \mathbf{U}_s^T \left[\xi^2 \mathbf{k}_{11} \mathbf{U}_{s,\xi\xi} + \xi (2\mathbf{k}_{11} + \mathbf{k}_{12} - \mathbf{k}_{21}) \mathbf{U}_{s,\xi} + (\mathbf{k}_{12} - \mathbf{k}_{22}) \mathbf{U}_s \right] d\xi \tag{29}$$

with $(\dots)_{,\xi} = \frac{\partial(\dots)}{\partial \xi}$. Let $\mathbf{B}_1 = \frac{1}{J} \mathbf{b}_\xi \mathbf{N}_s$ and $\mathbf{B}_2 = \frac{1}{J} (\mathbf{b}_\eta \mathbf{N}_{s,\eta} + \mathbf{b}_\zeta \mathbf{N}_{s,\zeta})$ and considering Eqs. (3) and (11), the coefficient matrices are given as

$$\mathbf{k}_{11} = \int_0^1 \int_0^1 \mathbf{B}_1^T \mathbf{C} \mathbf{B}_1 \bar{J} \, d\eta \, d\zeta \quad \mathbf{k}_{22} = \int_0^1 \int_0^1 \mathbf{B}_2^T \mathbf{C} \mathbf{B}_2 \bar{J} \, d\eta \, d\zeta \tag{30}$$

$$\mathbf{k}_{12} = \int_0^1 \int_0^1 \mathbf{B}_1^T \mathbf{C} \mathbf{B}_2 \bar{J} \, d\eta \, d\zeta \quad \mathbf{k}_{21} = \int_0^1 \int_0^1 \mathbf{B}_2^T \mathbf{C} \mathbf{B}_1 \bar{J} \, d\eta \, d\zeta .$$

The second term in Eq. (28) is rewritten considering Eqs. (A.4)–(A.6) to

$$\begin{aligned}
\int_{\partial\Omega_s} \delta \mathbf{u}^T \mathbf{t} \, dS &= \int_{S^\xi} \delta \mathbf{u}^T \mathbf{t}^\xi \, dS^\xi + \int_{S^\eta} \delta \mathbf{u}^T \mathbf{t}^\eta \, dS^\eta + \int_{S^\zeta} \delta \mathbf{u}^T \mathbf{t}^\zeta \, dS^\zeta \\
&= \delta \mathbf{U}_s^T \mathbf{F}_s \Big|_{\xi=0}^{\xi=1} + \int_0^1 \delta \mathbf{U}_s^T \xi \mathbf{T}_1 \, d\xi,
\end{aligned} \tag{31}$$

where the surfaces S^ξ , S^η , and S^ζ are illustrated in Fig. 3. The coefficient matrices \mathbf{F}_s and \mathbf{T}_1 are defined by

$$\begin{aligned}
\mathbf{F}_s &= \int_0^1 \int_0^1 \xi^2 \mathbf{N}_s^T \mathbf{t}^\xi \mathbf{g}^\xi \, d\eta \, d\zeta \\
\mathbf{T}_1 &= \int_0^1 \mathbf{N}_s^T \mathbf{t}^\zeta \mathbf{g}^\zeta \, d\eta \Big|_{\zeta=0}^{\zeta=1} + \int_0^1 \mathbf{N}_s^T \mathbf{t}^\eta \mathbf{g}^\eta \, d\zeta \Big|_{\eta=0}^{\eta=1}.
\end{aligned} \tag{32}$$

It should be noted that \mathbf{t}^ξ is identical to the prescribed traction $\bar{\mathbf{t}}$ on $\partial_t \Omega$ and that the force vector \mathbf{F}_s represents the nodal forces at the control points. After assembly over all sections \mathbf{T}_1 vanishes. With the help of Eq. (3), the third term in Eq. (28) is reformulated to

$$\int_{\Omega_s} \delta \mathbf{u}^T \rho \mathbf{b} \, dV = \int_0^1 \delta \mathbf{U}_s^T \xi^2 \mathbf{T}_2 \, d\xi \quad \text{with} \quad \mathbf{T}_2 = \int_0^1 \int_0^1 \mathbf{N}_s^T \rho \mathbf{b} \bar{\mathbf{J}} \, d\eta \, d\zeta. \tag{33}$$

Substituting Eqs. (29), (31), and (33) into the weak form of Eq. (28) yields

$$\begin{aligned}
&\sum_{s=1}^{nsec} \left(\delta \mathbf{U}_s^T (\xi^2 \mathbf{k}_{11} \mathbf{U}_{s,\xi} + \xi \mathbf{k}_{21} \mathbf{U}_s) \Big|_{\xi=0}^{\xi=1} - \right. \\
&\left. \sum_{s=1}^{nsec} \left(\int_0^1 \delta \mathbf{U}_s^T [\xi^2 \mathbf{k}_{11} \mathbf{U}_{s,\xi\xi} + \xi (2\mathbf{k}_{11} + \mathbf{k}_{12} - \mathbf{k}_{21}) \mathbf{U}_{s,\xi} + (\mathbf{k}_{12} - \mathbf{k}_{22}) \mathbf{U}_s] \, d\xi \right) \right. \\
&\left. - \sum_{s=1}^{nsec} \left(\delta \mathbf{U}_s^T \mathbf{F}_s \Big|_{\xi=0}^{\xi=1} + \int_0^1 \delta \mathbf{U}_s^T \xi \mathbf{T}_1 \, d\xi \right) - \sum_{s=1}^{nsec} \left(\int_0^1 \delta \mathbf{U}_s^T \xi^2 \mathbf{T}_2 \, d\xi \right) \right) = \mathbf{0}.
\end{aligned} \tag{34}$$

Collecting the boundary terms and the field equations leads to the following set of equations:

$$\mathbf{A}_{s=1}^{nsec} (\mathbf{k}_{11} \mathbf{U}_{s,\xi} + \mathbf{k}_{21} \mathbf{U}_s - \mathbf{F}_s) = \mathbf{0} \quad \text{on } \partial_t \Omega \tag{35}$$

$$\begin{aligned}
& \mathbf{A}_{s=1}^{nsec} \left(\xi^2 \mathbf{k}_{11} \mathbf{U}_{s,\xi\xi} + \xi (2\mathbf{k}_{11} + \mathbf{k}_{12} - \mathbf{k}_{21}) \mathbf{U}_{s,\xi} + (\mathbf{k}_{12} - \mathbf{k}_{22}) \mathbf{U}_s \right) \\
& + \mathbf{A}_{s=1}^{nsec} \left(\xi \mathbf{T}_1 + \xi^2 \mathbf{T}_2 \right) = \mathbf{0} \quad \text{in } \Omega,
\end{aligned} \tag{36}$$

where $\mathbf{A}_{s=1}^{nsec}$ is introduced as the assembly operator. Equation (36) is the so-called scaled boundary finite element equation, which is a second-order Euler-type ordinary differential equation (ODE). The displacement \mathbf{U}_s is a function of the radial scaling parameter ξ only. Here, it is worthwhile to note that the governing equation of elasticity has been weakly enforced in the circumferential direction, see Eqs. (28) and (34), but it remains strong in the radial scaling direction as shown in Eq. (36). For linear elasticity, a unique analytical solution exists and can be computed with the eigenvalue method. The interested reader is referred to the studies of Song and Wolf (1997, 1998) for further details on the solution procedure.

4.3 NURBS-Based Hybrid Collocation-Galerkin Method

In this Section, the NURBS-based hybrid collocation-Galerkin method (NURBS-HCGM) will be presented. In the scope of this approach, the weak form of equilibrium is applied only in the circumferential direction of the boundary. In the radial scaling direction, the equation is solved numerically by employing the collocation method. NURBS basis functions approximate the response in all parametric directions. The scaled boundary finite element equation can be derived analogously to Sect. 4.2. Hereafter, the B-splines approximation and the collocation in radial scaling direction will be discussed.

B-spline approximation in scaling direction In this approach, NURBS basis functions are employed to describe the geometry of the boundary. For brevity, we will only refer to the NURBS approximation for 3D problems here. For 2D problems, the formulas for the NURBS approximation could be derived similarly.

The NURBS basis functions $R_{(ij)}^{pq}(\eta, \zeta)$ in the circumferential direction are adopted from the geometry model following the boundary representation modeling technique in CAD, see also Sect. 4.1. They can be enriched via order elevation or knot insertion. The geometry is, therefore, described exactly. The interpolation function $N_s(\eta, \zeta)$ is employed for the approximation of the solution on the boundary as given in Eq. (27). Note that in contrast to Sect. 4.2, the sectional domain Ω_s is here approximated with NURBS basis functions on the boundary and also in the radial scaling direction. In the radial scaling direction, all weight factors are set to $w_r = 1$ since only straight lines are defined. Hence, B-splines are employed for the interpolation in the radial scaling direction. The displacement $\mathbf{U}_s(\xi)$ is only a function of the radial scaling parameter ξ . Hence, the univariate NURBS basis functions $R_r^t(\xi)$ are employed. The displacement in the radial scaling direction reads

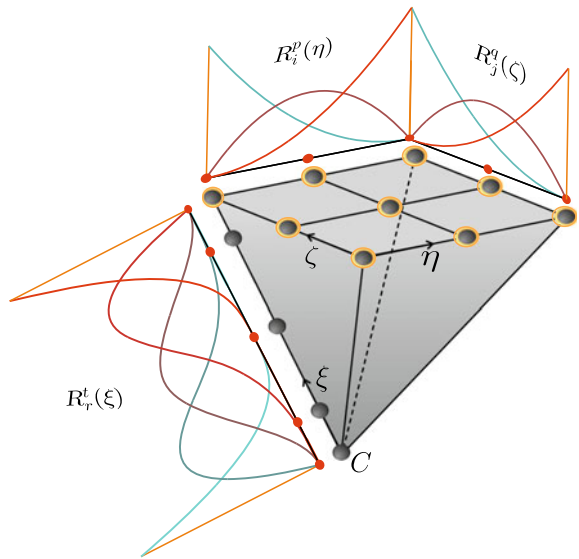
$$U_s(\xi) = \sum_{r=1}^{n_{cp}} R_r^t(\xi) U_{sr} \tag{37}$$

where the displacement vector U_{sr} is associated to the control points which are located in the radial scaling direction. The dimension of U_s and U_{sr} is $nds = 3 \cdot n_{bs}$ for 3D problems. n_{bs} is the total number of control points at the boundary of $\partial\Omega_s$. The polynomial degree in the radial scaling direction is denoted as t , and n_{cp} is the total number of control points per line in the radial scaling direction, see Fig. 7. The knot vector $\Xi = [\xi_1, \xi_2, \dots, \xi_{n_{cp}+t+1}]$ is employed to determine B-spline basis function R_r^t . Here, the radial scaling direction is represented by a straight line. The polynomial degree is $t = 1$ and the corresponding knot vector reads $\Xi = [0, 0, 1, 1]$. These are taken as the start values for further refinement by knot insertion or/and order elevation. In principle h -, p -, and k -refinement can be applied (Cottrell et al. 2009). Consequently, the number of control points n_{cp} is increased. Rearranging all control point vectors U_{sr} in the vector $U_{s\xi}$, the displacement Eq. (37) and the virtual displacement in the radial scaling direction could be rewritten as

$$U_s(\xi) = \underbrace{\begin{bmatrix} R_1^t & 0 & 0 & \dots & R_2^t & 0 & 0 & \dots & R_3^t & 0 & 0 & \dots \\ 0 & R_1^t & 0 & \dots & 0 & R_2^t & 0 & \dots & 0 & R_3^t & 0 & \dots \\ 0 & 0 & R_1^t & \dots & 0 & 0 & R_2^t & \dots & 0 & 0 & R_3^t & \dots \\ \vdots & \vdots & \vdots & \ddots & \vdots & \vdots & \vdots & \ddots & \vdots & \vdots & \vdots & \ddots \end{bmatrix}}_{N_\xi(\xi)} U_{s\xi}, \tag{38}$$

$$\delta U_s(\xi) = N_\xi(\xi) \delta U_{s\xi}.$$

Fig. 7 Illustration of NURBS basis functions in the parameter space for 3D problems. $n_{cp} = 5$ control points are used for the interpolation in the radial scaling direction. The B-splines $R_r^t(\xi)$ with $t = 3$ are shown only along one line in the radial scaling direction. All others radial lines are identical. $n_{bs} = 3 \times 3$ control points are employed in η and ζ directions. The boundary NURBS basis functions $R_i^p(\eta)$ and $R_j^q(\zeta)$ with $p = 2$ and $q = 2$ are shown



An example of the interpolation in the radial scaling direction and also in the circumferential direction is illustrated in Fig. 7 for a 3D problem. Taking into account the high continuity of the NURBS, the governing field equation (36) is approximated as

$$\begin{aligned} & \mathbf{A} \left(\sum_{r=1}^{n_{cp}} [\xi^2 \mathbf{k}_{11} R_r'' + \xi (2\mathbf{k}_{11} + \mathbf{k}_{12} - \mathbf{k}_{21}) R_r' + (\mathbf{k}_{12} - \mathbf{k}_{22}) R_r] U_r \right) \\ & + \mathbf{A} (\xi \mathbf{T}_1 + \xi^2 \mathbf{T}_2) = \mathbf{0} \quad \text{in } \Omega, \end{aligned} \quad (39)$$

where the abbreviation $(\dots)' = \frac{\partial(\dots)}{\partial\xi}$ is used. The approximation of the remaining Neumann boundary conditions in Eq. (35) is given by

$$\mathbf{A} \left(\sum_{r=1}^{n_{cp}} (\mathbf{k}_{11} R_r' + \mathbf{k}_{12} R_r) U_r - \mathbf{F}_s \right) = \mathbf{0} \quad \text{on } \partial_t \Omega. \quad (40)$$

Collocation In the scope of the NURBS-HCGM, the collocation method is employed to solve Equation (39) numerically. One collocation point per control point is sufficient in the framework of the NURBS-based collocation method, which can be interpreted as a rank sufficient one point quadrature as observed by Auricchio et al. (2012) and Schillinger et al. (2013). In the proposed method, only a one-dimensional ODE (Eqs. (35) and (36)) needs to be solved. In this case, the NURBS-based collocation method has been proved to be numerically stable (Auricchio et al. 2012), which motivates the use of NURBS for the approximation in scaling direction. The potential of the collocation method to solve differential equations has been widely investigated in the context of NURBS-based isogeometric analysis (for example, by Auricchio et al. 2010, 2012 and De Lorenzis et al. 2015 as well as Kiendl et al. 2015 and also Reali and Gomez 2015 and most recently Gomez and De Lorenzis 2016). Due to the above features, the NURBS-based collocation method is utilized to solve Eq. (39). The Greville abscissae is employed to define the collocation points. They are related to the knot vector $\Xi = [\xi_1, \xi_2, \dots, \xi_{n_{cp}+t+1}]$ as

$$\hat{\xi}_k = \frac{\xi_{k+1} + \xi_{k+2} + \dots + \xi_{k+t}}{t} \quad \text{for } k = 1, \dots, n_{cp}. \quad (41)$$

The first collocation point is located at the scaling center C with $\hat{\xi}_1 = 0$, while the last one is at the boundary with $\hat{\xi}_{n_{cp}} = 1$. As stated previously, the proposed method is a boundary-oriented method. Scaling the boundary surfaces yields the 3D solid. The unknown variables are the boundary degrees of freedom. If the first collocation point is chosen exactly at the scaling center C ($\hat{\xi}_1 = 0$), then numerical instabilities will arise. The physical explanation is that several control points will collapse to a single point (the scaling center C). This entails a rank deficiency of the final matrices in the collocation method. Equation (36) is a second-order Euler-type

ordinary differential equation (ODE) and its approximations is presented in Eq. (39). If the first collocation point is chosen exactly at the scaling center C ($\hat{\xi}_1 = 0$), then Eq. (39) reduces to

$$\mathbf{A}_{s=1}^{nsec} \left((\mathbf{k}_{12} - \mathbf{k}_{22}) R_r^t U_r \right) = \mathbf{0}. \quad (42)$$

Considering the property of the NURBS basis functions, $R_r^t(\hat{\xi}_1 = 0) = 1$ holds for the first control point. As a result, Eq. (42) can be rewritten to the homogeneous equation

$$(\mathbf{k}_{12} - \mathbf{k}_{22}) U_r(\hat{\xi}_1 = 0) = \mathbf{0}. \quad (43)$$

It will lead to either zero solutions or an infinite number of solutions at the scaling center C . However, both the solutions contradict to the prerequisite of finite solutions at the scaling center C . Hence, numerical instability will occur if the first collocation point coincides with the scaling center C ($\hat{\xi}_1 = 0$). To obviate this effect, a tolerance (tol) is introduced for the analysis and the first collocation point is defined as $\hat{\xi}_1 = 0 + tol$. The influence of the choice of the tolerance has been investigated by Chen et al. (2015). It has been observed that the results of the NURBS-HCG depend only very slightly on the choice of the first collocation point $\hat{\xi}_1$. There is only a marginal dependence between the accuracy of the approach and the choice for $\hat{\xi}_1$. Thus, the shifting of the first collocation point $\hat{\xi}_1$ can be allowed from a numerical point of view and the influence of this slight modification on the results can be neglected. In general, the first collocation point can be specified, for example, as $\hat{\xi}_1 = 0 + tol = 10^{-4}$.

The NURBS basis functions employed in the radial scaling direction are abbreviated as collocation NURBS. The displacement vector at the collocation points reads

$$U_s(\hat{\xi}_k) = \sum_{r=1}^{n_{cp}} R_r^t(\hat{\xi}_k) U_r = \sum_{r=1}^{n_{cp}} R_{rk}^t U_r. \quad (44)$$

The approximated Eq. (39) is reformulated for each collocation point except the one at the boundary. A system of $k = 1, \dots, n_{cp} - 1$ equations of the type

$$\begin{aligned} \mathbf{A}_{s=1}^{nsec} \left(\sum_{r=1}^{n_{cp}} \left[\hat{\xi}_k^2 \mathbf{k}_{11} R_{rk}^{t''} + \hat{\xi}_k (2\mathbf{k}_{11} + \mathbf{k}_{12} - \mathbf{k}_{21}) R_{rk}^{t'} + (\mathbf{k}_{12} - \mathbf{k}_{22}) R_{rk}^t \right] U_r \right) \\ + \mathbf{A}_{s=1}^{nsec} \left(\hat{\xi}_k T_1 + \hat{\xi}_k^2 T_2 \right) = \mathbf{0}. \end{aligned} \quad (45)$$

is established. At the boundary collocation point ($\hat{\xi}_{n_{cp}} = 1$), the Neumann boundary conditions defined in Eq. (40) are enforced by

$$\mathbf{A}_{s=1}^{nsec} \left(\sum_{r=1}^{n_{cp}} (\mathbf{k}_{11} R_{rn_{cp}}^{t'} + \mathbf{k}_{12} R_{rn_{cp}}^t) U_r - F_s \right) = \mathbf{0} \quad \text{on } \partial_t \Omega. \quad (46)$$

For a compact notation, the abbreviations $\bar{\mathbf{k}}_{r n_{cp}} = \mathbf{k}_{11}(R'_{r n_{cp}})' + \mathbf{k}_{12}R'_{r n_{cp}}$ and $\hat{\mathbf{k}}_{rk} = \hat{\xi}_k^2 \mathbf{k}_{11}R_{rk}'' + \hat{\xi}_k(2\mathbf{k}_{11} + \mathbf{k}_{12} - \mathbf{k}_{21})R_{rk}' + (\mathbf{k}_{12} - \mathbf{k}_{22})R_{rk}^t$ are introduced. After assembling over all sections of the domain Ω , \mathbf{T}_1 vanishes. The body forces \mathbf{T}_2 are neglected for the sake of simplicity. The system of equations constituted by Eqs. (45) and (46) is reformulated to

$$\begin{aligned} \mathbf{A} \left(\sum_{r=1}^{n_{cp}} \hat{\mathbf{k}}_{rk} \mathbf{U}_r \right) &= \mathbf{0} \quad k = 1, \dots, n_{cp} - 1, \\ \mathbf{A} \left(\sum_{r=1}^{n_{cp}} \bar{\mathbf{k}}_{r n_{cp}} \mathbf{U}_r - \mathbf{F}_s \right) &= \mathbf{0} \quad \text{on } \partial_t \Omega. \end{aligned} \quad (47)$$

The degrees of freedom located at the interior nodes are eliminated by static condensation. The degrees of freedom, located at the boundary $\partial\Omega$ are denoted as \mathbf{U} , while those associated with the interior of Ω are referred to as $\hat{\mathbf{U}}$. Let $\mathbf{F} = \sum_{s=1}^{n_{sec}} \mathbf{F}_s(\xi = 1)$, the system of equations reads

$$\begin{bmatrix} \hat{\mathbf{K}}_i & \hat{\mathbf{K}}_{ib} \\ \bar{\mathbf{K}}_{bi} & \bar{\mathbf{K}}_b \end{bmatrix} \begin{bmatrix} \hat{\mathbf{U}} \\ \mathbf{U} \end{bmatrix} - \begin{bmatrix} \mathbf{0} \\ \mathbf{F} \end{bmatrix} = \mathbf{0}, \quad (48)$$

where the subscripts b and i denote the matrices related to the boundary and the interior of Ω , respectively. The vector $\hat{\mathbf{U}}$ is eliminated from Eq. (48) by a static condensation. It results in the reduced system of equations

$$\mathbf{K}_\Omega \mathbf{U} + \mathbf{P}_\Omega = \mathbf{0} \quad (49)$$

with $\mathbf{K}_\Omega = \bar{\mathbf{K}}_b - \bar{\mathbf{K}}_{bi} \hat{\mathbf{K}}_i^{-1} \hat{\mathbf{K}}_{ib}$ and $\mathbf{P}_\Omega = -\mathbf{F}$. Equation (35) represents the weak form of the Neumann boundary conditions. De Lorenzis et al. (2015) observed that the imposition of the Neumann boundary conditions in a weak sense produces significantly lower error levels in comparison to a collocation-based evaluation of the Neumann boundary conditions. The Dirichlet boundary conditions are directly applied to the control points at the boundary. Hence, simply columns and rows of Eq. (49) are deleted. Solving Equation (49) yields the displacement \mathbf{U} of the control points at the boundary. All nodal displacements \mathbf{U}_s of a section can be determined using Eqs. (48) and (37). The displacement vector of an arbitrary point in Ω_s is given by Eq. (27). The strains and stresses are identified by Eqs. (5) and (6). It is noted that the displacement \mathbf{U} of the boundary control points is the essential variable in the whole algorithm. All other variables can be derived from it. Hence, the displacement solution at the boundary can be employed to evaluate the performance of this approach. In general, NURBS-HCGM solves the ODE defined by Eqs. (35) and (36) numerically due to the NURBS approximation in the radial scaling direction. The approximation of the displacement in the radial scaling direction allows the analysis of both linear and nonlinear problems. For linear problems, the ODE is directly solved by the col-

location method. While for nonlinear analysis, the Newton–Raphson scheme can be employed to solve the equilibrium equations iteratively. The presented formulation is suitable for the analysis of star-shaped solids. To deal with complex geometries, the finite element discretization could be employed to discretize the solid into numerous star-shaped macro elements. The stiffness matrix and the right-hand side for each macro element can be derived as in Eq. (49). This provides a macro element formulation for the general analysis of solids.

4.4 NURBS-Based Galerkin Method

In this Section, the NURBS-based Galerkin method (NURBS-G) will be presented. In the scope of this approach, the weak form of equilibrium equation is applied in all parametric directions of the solid. Hereafter, the NURBS approximation and the derivation of the weak form of the equilibrium equation will be addressed.

NURBS Approximation In this approach, NURBS basis functions are employed to describe the geometry of the boundary, see Sect. 4.1. The approximation is done analogously to the NURBS-HCGM, see Sect. 4.3, which means that the interpolation at the boundary is done with the NURBS basis functions of the geometry whereas in the interior it is done with B-Splines. An example of the interpolation in the radial scaling direction and also in the circumferential direction is illustrated in Fig. 7 for a 3D problem. Here, it is worthwhile to note that the stiffness matrix of the NURBS-G can be alternatively obtained by modifying the geometry of a rectangular patch to a triangle. An example is illustrated in Fig. 8 for the 2D case. In the following, the derivation of the stiffness matrix with the original geometry of the boundary as the starting point for the analysis will be demonstrated.

Weak Form of Equilibrium Equation In this Section, the weak form of equilibrium is derived for the 3D case. For 2D problems, the weak form of equilibrium equation could be obtained analogously. The difference to the procedure in Section 4.3 is that the weak form is employed in all parametric directions. Also here, we employ the principle of virtual work to derive the Eq. (28). Consequently, the first term of Eq. (28) represents the internal virtual work, the second term is the external virtual work

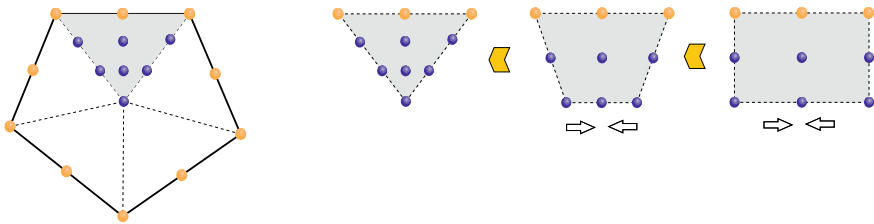


Fig. 8 Derivation of a triangular patch by modifying the geometry in 2D

done by the boundary tractions, and the third term is the external virtual work done by the body forces. The virtual strains are given also as $\delta \boldsymbol{\varepsilon} = \mathbf{D}^T \delta \mathbf{u}(\xi, \eta, \zeta)$. The approximation of the displacements and the virtual displacements on the sectional domain Ω_s is defined according to Eq. (27). Note that the sectional domain Ω_s is approximated with NURBS on the boundary as well as in the radial scaling direction. The stress vector is computed by $\boldsymbol{\sigma} = \mathbb{C} \mathbf{D}^T \mathbf{u}$ using Eqs. (5) and (6). The first term in Eq. (28) is rewritten by expanding the integral

$$\begin{aligned} \int_{\Omega_s} \delta \boldsymbol{\varepsilon}^T \boldsymbol{\sigma} \, dV &= \int_0^1 \delta \mathbf{U}_s^T \cdot_{,\xi} \xi^2 \mathbf{k}_{11} \mathbf{U}_{s,\xi} \, d\xi + \int_0^1 \delta \mathbf{U}_s^T \cdot_{,\xi} \xi \mathbf{k}_{12} \mathbf{U}_s \, d\xi \\ &+ \int_0^1 \delta \mathbf{U}_s^T \xi \mathbf{k}_{21} \mathbf{U}_{s,\xi} \, d\xi + \int_0^1 \delta \mathbf{U}_s^T \mathbf{k}_{22} \mathbf{U}_s \, d\xi \end{aligned} \quad (50)$$

with $(\dots)_{,\xi} = \frac{\partial(\dots)}{\partial \xi}$. The coefficient matrices are given in Eq. (30). The second term in Eq. (28) is rewritten by considering Eqs. (A.4)–(A.6) to Eq. (31). The coefficient matrices for the right-hand side are defined in Eq. (32). With the help of Eq. (3), the third term in Eq. (28) is reformulated to Eq. (33). Substituting Eqs. (50), (31), and (33) into Eq. (28) leads to the weak form of equilibrium equation for 3D problems

$$\begin{aligned} \sum_{s=1}^{nsec} \left(\int_0^1 \delta \mathbf{U}_s^T \cdot_{,\xi} (\xi^2 \mathbf{k}_{11} \mathbf{U}_{s,\xi} + \xi \mathbf{k}_{12} \mathbf{U}_s) \, d\xi + \int_0^1 \delta \mathbf{U}_s^T (\xi \mathbf{k}_{21} \mathbf{U}_{s,\xi} + \mathbf{k}_{22} \mathbf{U}_s) \, d\xi \right) \\ - \sum_{s=1}^{nsec} \left(\delta \mathbf{U}_s^T \mathbf{F}_s \Big|_{\xi=0}^{\xi=1} - \int_0^1 \delta \mathbf{U}_s^T \xi^2 \mathbf{T}_1 \, d\xi \right) = \mathbf{0}. \end{aligned} \quad (51)$$

If the stress resultants in Eq. (28) are replaced with the Cauchy stress, the formulations here are suitable for the geometrical nonlinear analysis. Also, the stress–strain constitutive relation is flexible in these equations, thus, material nonlinearities can be considered (Chasapi and Klinkel 2018).

Substituting Eq. (38) into (51) yields the compact form of the weak form of equilibrium equation for 3D problems. For the sake of simplicity the body forces \mathbf{T}_2 are neglected. The system of equations is written as

$$\delta \mathbf{U}_\xi^T (\mathbf{F}_\Omega - \mathbf{K}_\Omega \mathbf{U}_\xi) = \mathbf{0} \quad \text{with} \quad \mathbf{U}_\xi = \mathbf{A}_{s=1}^{nsec} (\mathbf{U}_{s\xi}) \quad (52)$$

where $\mathbf{A}_{s=1}^{nsec}$ is the assembly operator to assemble the variables over all the sectional domains. \mathbf{K}_Ω is the stiffness matrix of the entire domain. \mathbf{U}_ξ is the nodal displacement in the entire domain. The coefficient matrices are given as

$$\begin{aligned}
 \mathbf{F}_\Omega &= \mathbf{A} \underset{s=1}{\overset{nsec}{\mathbf{F}}}_s \left[\begin{array}{c} \mathbf{0} \\ \mathbf{F}_s (\xi = 1) \end{array} \right] \\
 \mathbf{K}_\Omega &= \mathbf{A} \left(\int_0^1 \left[\mathbf{N}_{\xi, \xi}^T (\xi^2 \mathbf{k}_{11} N_{\xi, \xi} + \xi \mathbf{k}_{12} N_\xi) + \mathbf{N}_\xi^T (\xi \mathbf{k}_{21} N_{\xi, \xi} + \mathbf{k}_{22} N_\xi) \right] d\xi \right)
 \end{aligned} \tag{53}$$

For arbitrary test functions $\delta \mathbf{U}_\xi$ in Eq. (52), the global system of equilibrium equations can be obtained as

$$\mathbf{K}_\Omega \mathbf{U}_\xi - \mathbf{F}_\Omega = \mathbf{0}. \tag{54}$$

The degrees of freedom located at the interior nodes are eliminated by static condensation from Eq. (54). The degrees of freedom, located at the boundary $\partial\Omega$, are denoted as \mathbf{U} , while those associated with the interior of Ω are referred as $\hat{\mathbf{U}}$. Let $\mathbf{F} = \mathbf{A} \underset{s=1}{\overset{nsec}{\mathbf{F}}}_s (\xi = 1)$, the system of equations is given in Eq. (48). The vector $\hat{\mathbf{U}}$ is eliminated from Eq. (48) by a static condensation. This results in a reduced system of equations, which only relates to the boundary degrees of freedom, see Eq. (49).

Until now, all the formulations for the isogeometric analysis of solids in boundary representation are available. To sum up, the solid is divided in the analysis into several sectional domains Ω_s . This division is in principle flexible. For the following numerical examples, C_0 continuity at the boundary is, however, employed to divide the solid. NURBS basis functions are employed for the description of the boundary geometry as well as for the approximation of the displacements at the boundary, see Eqs. (24) and (27). The interior of the domain is described by a scaling center and a radial scaling parameter. The scaling center is chosen in a zone from which the total boundary of the domain is visible (Song and Wolf 1997). The scaling center will, in general, be located inside the domain. It could be defined as the geometric center of the domain if it is convenient to obtain. Or it could be defined as the average coordinate of the control points which are used to define the total boundary of the domain. The displacement in the radial scaling direction is approximated by a one-dimensional B-spline basis function, which is the main difference to the semi-analytical approach where the analytical solution in the scaling direction is employed. The approximation of the displacement in the radial scaling direction allows for the analysis of both linear and nonlinear problems. Applying the weak form to the governing partial differential equation of elasticity, the global system of equilibrium equation is obtained, see Eq. (47). The Galerkin or the collocation method can be employed in the radial scaling direction to solve the ODE. The Dirichlet boundary conditions are directly applied to the control points at the boundary. Hence, simply columns and rows of Eq. (48) are deleted. Solving Equation (48) yields the displacement \mathbf{U} of the control points at the boundary. All nodal displacements \mathbf{U}_s of a section can be determined by using Eqs. (38) and (47). The displacement vector at an arbitrary point in Ω_s is given by Eq. (27). The strains and stresses are identified by Eqs. (5) and (6). The above- presented analysis procedures are surface-oriented methods. They are suitable for the numerical analysis if only the geometry of the boundary surfaces is

given. This is the case with solids, which are designed in CAD with the boundary representation modeling technique. The choice of the method depends on the problem under investigation. In the following, the methods are discussed in terms of accuracy and efficiency. A comparison between the presented formulations and also with standard numerical methods is provided.

5 Numerical Examples

In this Section, five numerical examples related to 2D and 3D elastic problems will be presented. All examples are employed to demonstrate the capabilities of the NURBS-based hybrid Galerkin-collocation method (NURBS-HCGM) and the NURBS-based Galerkin method (NURBS-G). The first two examples are employed to demonstrate the performance in terms of accuracy. Hence, an extensive comparison between both methods as well as a comparison to standard isogeometric analysis (IGA) is considered. The last three examples are presented to illustrate the capability of the methods. Therefore, a comparison with standard FEM and IGA are presented. For all examples, each sectional domain is modeled with the same NURBS basis functions, which employ identical polynomial degree and knot vector. However, it should be noted that the choice of the polynomial degree and the knot vector to approximate each boundary is in principle flexible. Moreover, all 3D computational meshes considered are conforming, which means that adjacent surface patches employ the same polynomial degree and knot vector along the shared edge. However, the NURBS description of boundary surfaces is in principle flexible. Methods for the coupling of nonconforming meshes which could be employed for the analysis are given by Apostolatos et al. (2014), Ruess et al. (2014), and Dornisch et al. (2015). A further extension could be the treatment of trimmed boundary surfaces (Schmidt et al. 2012; Breitenberger et al. 2015).

In the linear analysis, the problems can be solved analytically by employing the eigenvalue approach (Song and Wolf 1997). Here, the eigenvalue solution is used as an optimal solution to evaluate the accuracy of the NURBS-G and NURBS-HCGM. In the eigenvalue method, the unknown variables are the displacements $\tilde{\mathbf{U}}$ of boundary control points. For the numerical examples, we will mainly focus on the error investigation of the boundary displacement $\tilde{\mathbf{U}}$.

Declarations for the description of solids are summarized in Table 1. The NURBS basis functions employed to describe the boundary are termed as boundary NURBS. The corresponding control points are denoted as boundary control points. Analogously, the NURBS basis functions used in the radial scaling direction are abbreviated as radial or collocation NURBS and the control points are denoted as radial control points or collocations points in case of the NURBS-HCGM. \mathbf{u}_α ($\alpha = eg, an, cl$) represents the displacement obtained by the eigenvalue method, the analytical solution and the NURBS-G or NURBS-HCGM, respectively. The vectors \mathbf{u}_α^g ($\alpha = eg, an, cl$) denote the displacement of boundary Gauss integration points used in the integrals of Eq. (30).

Table 1 Nomenclature to define the numerical models

Parameter	Description
p_B	Polynomial degree of boundary NURBS ($p_B = p = q$)
N_B	Total number of boundary control points
$p_C = t$ $N_C = n_{cp}$	Polynomial degree of radial or collocation NURBS, Eq. (37) number of control points or collocation points per line in the radial scaling direction, Eq. (37), abbreviated as number of radial control points or collocations points

The relative error of displacement response is computed with the aid of L^∞ -norm. With respect to the displacements at the boundary, the norm is defined as

$$\|\mathbf{v}\|_{L^\infty(\partial\Omega)} = \max |\mathbf{v}| \quad \forall \mathbf{v} \in L^\infty(\partial\Omega) . \quad (55)$$

This error measure is employed in convergence studies, where mesh refinement and order elevation are considered. It is distinguished between a refinement for the radial scaling direction and for the boundary. The influence of the polynomial degree of radial NURBS and the number of radial control points on the accuracy is investigated for a fixed boundary discretization. An optimal solution is gained by using the eigenvalue method (Song and Wolf 1997). In the next step, the influence of boundary description is discussed. The polynomial degree of boundary NURBS and the number of boundary control points affect the accuracy of the displacement response. Here, optimal rules for the choice of all parameters are provided. Moreover, the capability of the analysis procedures is illustrated by comparison to standard numerical methods. Within the numerical examples, analytical solutions serve as a reference to evaluate the error.

5.1 Infinite Plate with Circular Hole

The aim of this example is to study the convergence behavior of the eigenvalue method, the NURBS-G and the NURBS-HCGM for 2D problems. The geometry and boundary conditions of the plate are illustrated in Fig. 9. Due to the symmetry, only one-quarter of the plate is modeled. The exact traction from the analytical solution is imposed at the free boundary (Apostolatos et al. 2014). The material properties are considered with the Young's modulus $E = 100 \text{ N/m}^2$, the Poisson's ratio $\nu = 0.3$, and the thickness $h = 1 \text{ m}$. The eigenvalue method as well as the NURBS-HCGM and NURBS-G are employed in the analysis. Here, the plate is divided into five sections with respect to the scaling center, which are bounded by dashed lines, see Fig. 9. The scaling center C is defined by the average of all control points at the boundary. The boundary of each section Ω_s is discretized with the initial polynomial degree $p_B = 2$ and with the initial knot vector $\mathbf{H} = [0, 0, 0, 1, 1, 1]$. The polynomial

Fig. 9 Infinite plate with circular hole: problem definition

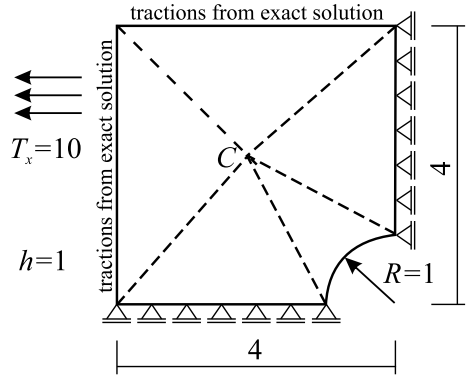
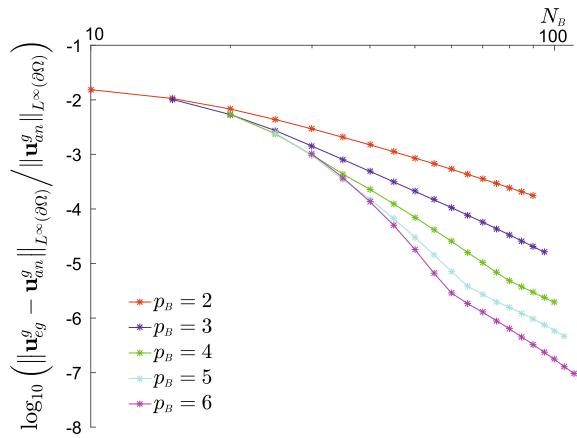


Fig. 10 Relative error of the displacement at the boundary $\partial\Omega$ for eigenvalue method



degree is increased by order elevation. The number of elements is increased for a fixed polynomial degree by h -refinement of the open knot vector. Correspondingly, the total number of boundary control points N_B is increased.

Solution of the eigenvalue method A solution for a given discretization of the boundary is calculated by the eigenvalue method (Song and Wolf 1997). As this method leads to an analytical solution for linear problems, it serves as a reference solution for the evaluation of the NURBS-G and NURBS-HCG. In this method, the decisive parameters which influence the accuracy are the polynomial degree p_B and the total number of boundary control points N_B . Here, the convergence of the displacement at the boundary $\partial\Omega$ in the L^∞ -norm is investigated, see Fig. 10. As it can be seen in the figure, the eigenvalue method performs accurately. It leads to the exact solution with increasing polynomial degree of boundary NURBS and total number of boundary control points.

Solution of the NURBS-HCGM and NURBS-G The accuracy of the presented numerical methods is not only determined by the parameters of boundary NURBS

(p_B and N_B), but also by the parameters of radial NURBS (p_C and N_C). Hence, the following convergence studies are performed for different choices of p_B , N_B , p_C and N_C .

Since the analysis is linear, first we consider the solution of the eigenvalue method as the reference solution for the convergence study. Within this study, the performance of the presented methods concerning the accuracy of the displacement with respect to the eigenvalue method will be investigated. The L^∞ error norm for the displacement will be employed. For better illustration, we present a comparison of the NURBS-based Galerkin (NURBS-G) with the hybrid collocation-Galerkin method (NURBS-HCGM) in terms of computational efficiency and accuracy. In the NURBS-HCGM, the same boundary description as the NURBS-G is employed, however, the equation in the radial scaling direction is solved by the NURBS-based collocation method. In the frame of NURBS-based analysis, extensive studies regarding the collocation method are presented by Auricchio et al. (2012), De Lorenzis et al. (2015), Kiendl et al. (2015), Reali and Gomez (2015), Klinkel et al. (2015), and Chen et al. (2015). Furthermore, the convergence of the NURBS-G relative to the analytical solution is presented by means of the L^∞ error norm. Here, we will compare the NURBS-G with the standard Galerkin-based isogeometric analysis (IGA) in terms of their accuracy against the analytical solution.

(a) Influence of the parameters in the radial scaling direction

Figure 11 presents convergence plots for the displacement at the boundary of domain Ω . A comparison of the displacements obtained by the NURBS-G and the NURBS-HCGM relative to those by the eigenvalue method is presented. The L^∞

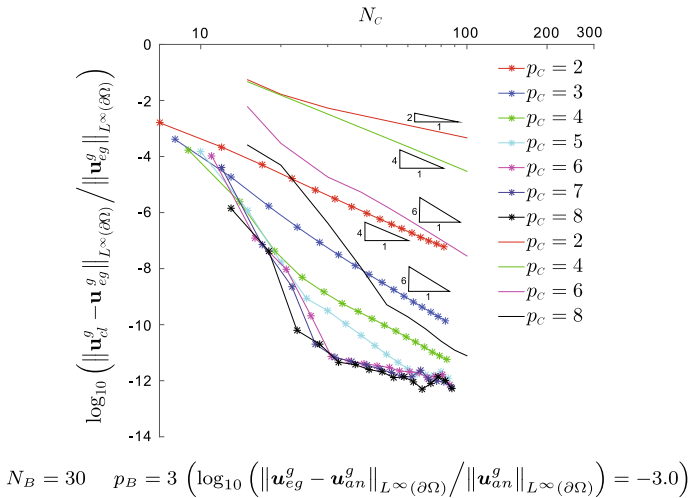


Fig. 11 Relative error of the displacement at the boundary $\partial\Omega$ for NURBS-G denoted with lines & star and NURBS-HCGM denoted with solid lines: different polynomial degrees of radial NURBS and number of radial control points are concerned

error norm for the displacement at the boundary Gauss integration points is considered in the comparison. For a fixed boundary description (i.e., p_B and N_B are fixed), different polynomial degrees of radial NURBS p_C and number of radial control points N_C are utilized in the convergence study. In the figures, the results of the NURBS-G are denoted as line with stars, while the results of the NURBS-HCGM are represented as solid lines. For the NURBS-HCGM, only the results of even polynomial degree of radial NURBS are presented, because the best possible convergence rates are attained for even degrees in the NURBS-HCGM (Klinkel et al. 2015; Schillinger et al. 2013). In addition, to illustrate the best possible accuracy under current boundary description, the relative error between the eigenvalue method and the analytical solution is shown in the caption of Fig. 11. It can be seen, that the accuracy of both methods increases with increasing polynomial degree and number of radial control points. The error level of the proposed NURBS-G is comparably lower than that of the NURBS-HCGM in terms of the control points and the polynomial degree of radial NURBS. For a specified level of accuracy within the NURBS-HCGM, the polynomial degree of radial NURBS should satisfy $p_C \geq \text{even}(p_B)$ and the number of radial points $N_C \geq N_B$. A further advantage of the NURBS-G is that there is no singularity arising at the scaling center compared to the NURBS-HCGM, hence the solution procedure is stable (see also Klinkel et al. 2015; Chen et al. 2015).

(b) Influence of the parameters in the circumferential direction

The rate of convergence is independent of the polynomial degree of boundary NURBS in the presented NURBS-G as well as NURBS-HCGM method. Greater difference between p_B and p_C will lead, however, to more accurate results for a given number of radial points. The same holds also for the total number of boundary control points, when the same polynomial degree of radial NURBS is concerned. Here also, greater difference between N_B and N_C will yield better results provided that the same number of radial points N_C is employed in the computation. The reader is referred to the studies of Klinkel et al. (2015) and Chen et al. (2015, 2016) for further numerical results.

(c) Comparison of the NURBS-G with the isogeometric analysis (IGA)

Here, the boundary of each section Ω_i is described by NURBS basis functions with identical polynomial degree p_B . It employs $p_B = 2$ with the initial open knot vector $\mathbf{H} = [0, 0, 0, 1, 1, 1]$, and extends to $p_B = 3, 4, 5$, and 6, respectively. Under each polynomial degree of boundary NURBS, the number of elements along the boundary of each section is initially $n = 1$, and extends to $n = 2, 3, 4, 5, 6, 7$, and 8, separately. The h -refinement of the open knot vector is employed to generate new open knot vectors. The total number of boundary control points N_B is increased, respectively. To illustrate the capability of the NURBS-G, we provide a comparison to the isogeometric analysis (Dornisch et al. 2013). In Fig. 12, the different meshing strategies of both approaches are depicted. For the NURBS-G model, the scaling center C is defined by the average of the coordinates of the boundary control points, which are denoted as red dots in the figure. The plate is modeled by five sections,

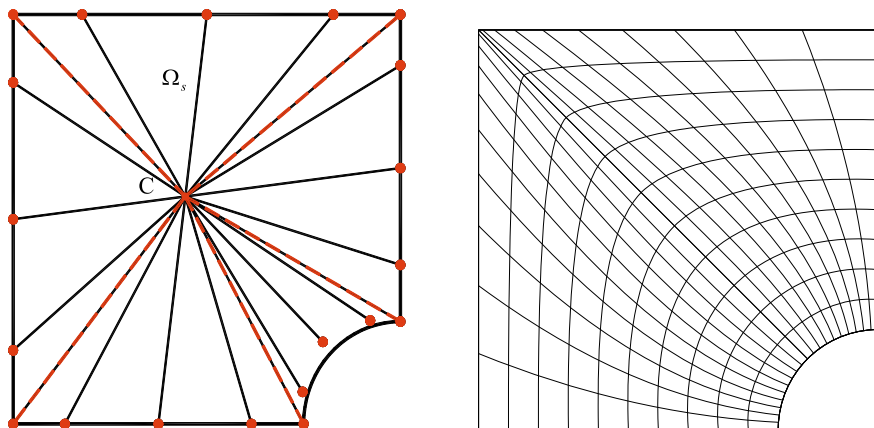
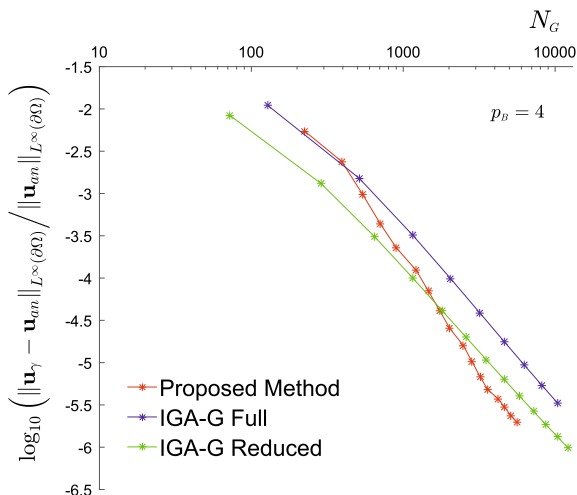


Fig. 12 On the left-hand side, the mesh of the NURBS-based Galerkin method and on the right-hand side the mesh of the isogeometric Galerkin approach are depicted

Fig. 13 L^∞ error norm of the displacement at the boundary $\partial\Omega$: different polynomial degrees of boundary NURBS and total numbers of Gauss integration points are considered



where each section Ω_s is bounded by red colored dashed lines. For the IGA, k -refinement of the open knot vector is employed to generate new open knot vectors.

In Fig. 13, the L^∞ error norm for the displacement at the boundary is employed to demonstrate the accuracy of the NURBS-G approach. In the figure, \mathbf{u}_γ denotes the displacement solution obtained from the NURBS-G and the IGA approach, respectively. For the NURBS-G, the polynomial degree of radial NURBS is defined as $p_c = p_B$. The number of radial control points is set as $N_c = \text{ceil}(N_B/4) + p_c$. Here, $\text{ceil}(\cdot)$ denotes the round-toward-infinity function. In the NURBS-G, the reduced quadrature with $\text{ceil}(p_c/2)+1$ Gauss points per element is employed to perform the integration. In the IGA approach, two integration strategies are employed for the

Gauss quadrature integration: full quadrature with $p_B + 1$ Gauss points per element and reduced quadrature with $\text{ceil}(p_B/2)+1$ Gauss points per element (Hughes et al. 2010). In the figures, the relative L^∞ error norm is plotted versus the total number of Gauss points N_G employed in the NURBS-G and IGA approach, respectively.

Concerning the accuracy of the NURBS-G, it can be seen in Fig. 13 that the method performs accurately. It leads to the exact solution with the rise of polynomial degree of boundary NURBS and total number of Gauss points. Additionally, the proposed NURBS-G and IGA yield error levels in the same range in terms of total integration points. For coarse discretizations, the IGA performs better than the NURBS-G, for finer discretizations the NURBS-G slightly outperforms the IGA.

5.2 Solid Sphere Under Hydrostatic Pressure

The aim of this example is to investigate the rate of convergence of the NURBS-G and NURBS-HCG for 3D problems. Due to the symmetry of the system, only one-eighth of the solid sphere is modeled. The geometry is shown in Fig. 14. The radius of the sphere is $R_b = 10$ m. In the analysis, the solid sphere is modeled by four sections, which are bounded by the curved boundary surfaces as shown in Fig. 14c. One section Ω_s is shown in Fig. 14c and indicated by dashed lines. The scaling center C is defined by the centroid of the sphere. The boundary surface of each sectional domain Ω_s is initially described by the polynomial degree $p_B = 2$ and the knot vectors $\mathbf{H} = \mathbf{Z} = [0, 0, 0, 1, 1, 1]$. The polynomial degree is increased by using k -refinement. The number of elements is increased for a fixed polynomial degree by h -refinement of the open knot vector. An example of the control polygon and mesh of the boundary surfaces is presented in Fig. 15, which employs the knot vector $\mathbf{H} = \mathbf{Z} = [0, 0, 0, 0.5, 1, 1, 1]$ and the polynomial degree $p_B = 2$. The system is loaded by hydrostatic pressure, which is imposed at the external spherical surfaces. The analytical solution for the displacement and the stress of the solid sphere is given

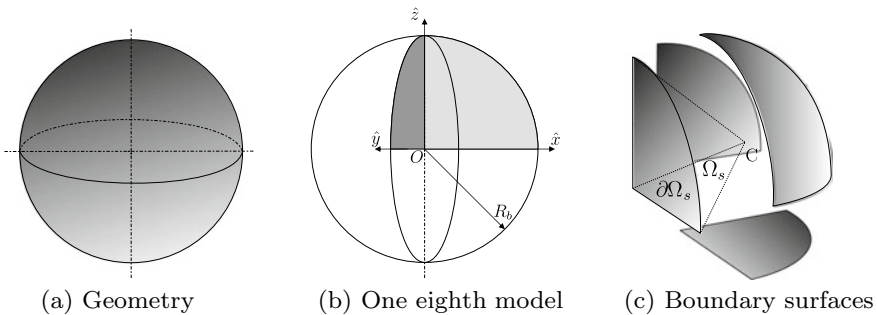


Fig. 14 Solid sphere: problem definition and boundary description

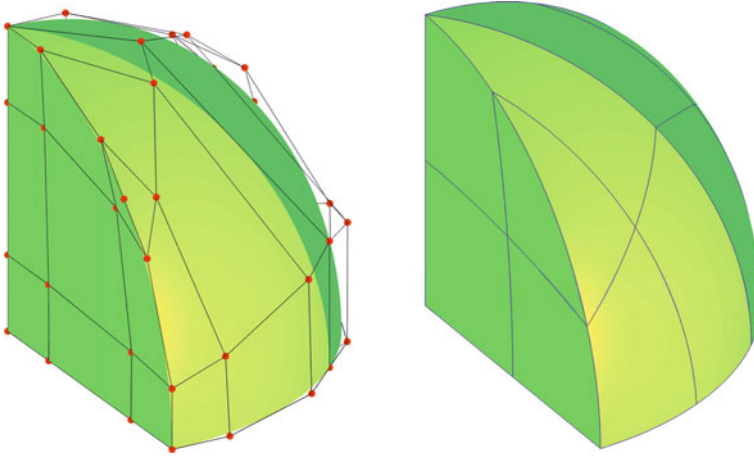


Fig. 15 Control polygon and mesh on the boundary surfaces of the solid sphere ($p_b = 2$ and 2 elements per parametric direction)

by Timoshenko (1951). Considering the spherical coordinates (r, ϕ, θ) , the radial displacement and stress read

$$u_r = -\frac{(1-2\nu)r}{E}q_b \quad \sigma_r = -q_b \quad (56)$$

with the external hydrostatic pressure q_b . The material properties of the sphere are: Young's modulus $E = 100 \text{ N/m}^2$ and Poisson's ratio $\nu = 0.0$. The external hydrostatic pressure is $q_b = 10 \text{ N/m}^2$. In the following, the eigenvalue method as well as the NURBS-G and NURBS-HCGM are employed for the analysis.

Solution of the eigenvalue method Here, the convergence of the displacement at the boundary surface $\partial\Omega$ in the L^∞ error norm is investigated by employing the eigenvalue method (Song and Wolf 1997). Figure 16 shows that the degree elevation and knot insertion lead to converged results. In analogy with the previous example, the eigenvalue method serves as reference solution in the linear elastic case.

Solution of the NURBS-HCG and NURBS-G For better illustration, an extensive comparison of the NURBS-G with the NURBS-HCGM is presented with respect to their computational efficiency and accuracy. In addition to the comparison between the NURBS-HCG and NURBS-G, the accuracy and efficiency of the NURBS-HCG are further investigated in detail. Finally, the accuracy of both methods with respect to the analytical solution will be discussed.

For a given boundary surface discretization, defined by N_b and p_b , the efficiency and accuracy of the methods also depend on the polynomial degree of radial NURBS p_c and the number of radial control points N_c . A convergence study will be, therefore, performed for different choices of p_b , N_b , p_c , and N_c in analogy with the previous 2D example. In the following, the L^∞ error norm for displacements will be employed.

Fig. 16 Relative error of the displacement at the boundary $\partial\Omega$ of the solid sphere (solution of the eigenvalue method)

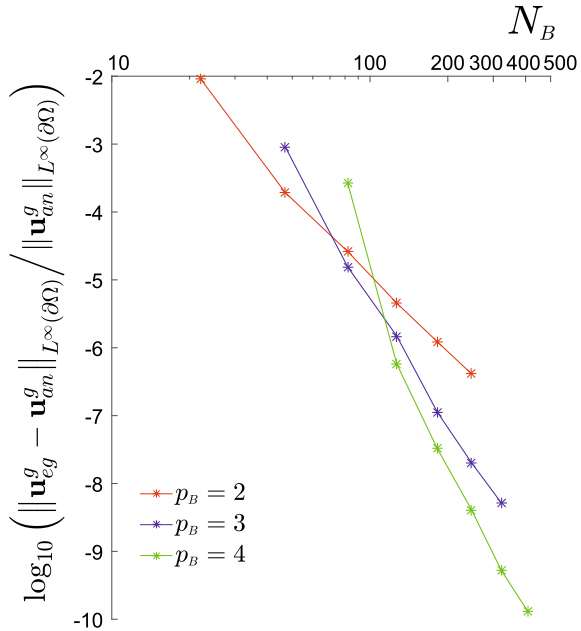


Figure 17 presents the convergence plots for displacements at the boundary Gauss integration points. For a fixed boundary description, different polynomial degree of radial NURBS p_c and number of radial control points N_c are employed. The solution of the eigenvalue method is set as the reference solution. Thus, the relative error between the eigenvalue method, the NURBS-G and the NURBS-HCGM is displayed in Fig. 17. In the figures, the lines with stars denote the results of the NURBS-G, while solid lines represent the results of the NURBS-HCGM. For the NURBS-HCGM, only the results of even polynomial of radial NURBS are presented in order to achieve best possible convergence rates (Chen et al. 2015). The best possible accuracy under current boundary description is given as the relative error between the eigenvalue method and the analytical solution with the L^∞ error norm, see Fig. 17.

It can be seen in the figure that both the NURBS-HCG and NURBS-G converge with increasing p_c . The error level of the NURBS-G is comparably lower than that of the NURBS-HCGM. In the figure, it can be observed that a rate of convergence $2p_c$ is attained in the L^∞ -norm, which can be considered as the best possible rate of convergence. Although the solution for high polynomial degrees indicates instabilities for fine discretizations, note that these results are already converged at the machine precision under consideration of the conditioning of the matrix.

(a) Influence of the parameters in radial scaling direction on the accuracy of the NURBS-HCGM

Figure 18 presents convergence plots for the displacement at the boundary Gauss integration points, which illustrate the influence of collocation. For a fixed polynomial

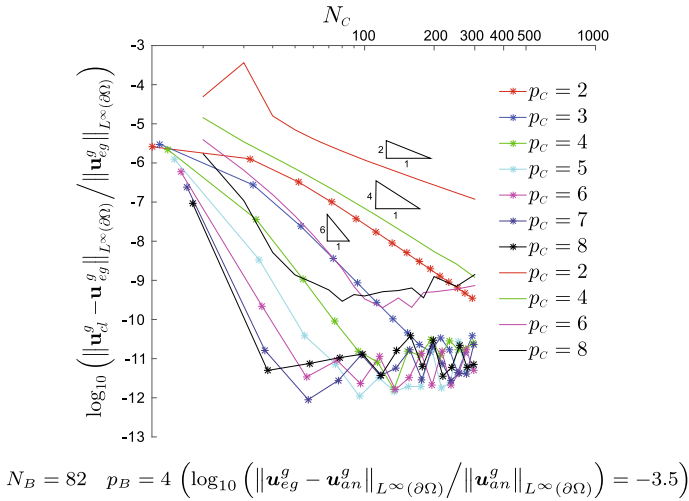


Fig. 17 Relative error of the displacement at the boundary $\partial\Omega$ for NURBS-G denoted with lines & stars and NURBS-HCGM denoted with solid lines with respect to the solution of the eigenvalue method: The influence of the polynomial degree of radial NURBS is examined for a fixed boundary discretization

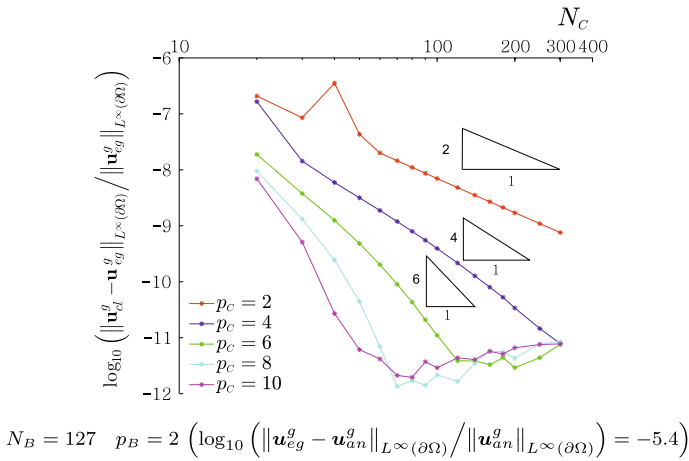


Fig. 18 Relative error of the displacement at the boundary $\partial\Omega$ (solution of the NURBS-HCGM compared to the eigenvalue method): The influence of the polynomial degree of the collocation NURBS is examined for a fixed boundary discretization

degree of boundary NURBS and a fixed total number of boundary control points, different polynomial degrees of collocation NURBS p_c and numbers of collocation points N_c are utilized. Here, the solution of the eigenvalue method is set as the reference solution. Thus, the relative error between the eigenvalue method and the NURBS-HCGM is displayed in Fig. 18. The L^∞ -norm of the error is employed for the comparison. In the figure, only the results of even polynomial degrees of collocation NURBS are presented for better illustration. The results given in Fig. 18 show that the displacements converge for increasing polynomial degrees p_c . A rate of convergence p_c is attained for even degrees.

This is consistent with the observations of Auricchio et al. (2010) and can be referred to as the best possible convergence rates. Although unstable results are attained for very high polynomial degrees and number of collocation points, note that these results are already converged at the machine precision under consideration of the conditioning of the matrix.

Figure 18 demonstrates that also an increase of the number of collocation points N_c results in a higher accuracy. However, unstable results are also obtained on the convergence line before it attains the corresponding rate of convergence. The turning point is approximately observed at $N_c \approx N_B/2$. The following two rules are, therefore, suggested to achieve a stable collocation with the best possible convergence behavior:

1. The number of collocation points should satisfy $N_c \geq N_B/2$ to avoid unstable results on the convergence lines.
2. The polynomial degree of collocation NURBS should be set to $p_c \geq \text{even}(p_B)$, where $\text{even}(A)$ rounds A to the nearest even number greater than or equal to A . Higher difference between p_c and p_B will lead to more accurate results.

These rules may underestimate the accuracy of the NURBS-HCGM for some lower polynomial degrees of collocation NURBS and number of collocation points. However, they provide the best possible accuracy of the method.

(b) Influence of the parameters in the circumferential direction of the boundary on the accuracy of the NURBS-HCGM

As the same polynomial degree of collocation NURBS p_c is concerned, the rate of convergence is identical for the different choices of p_B , which implies that the rate of convergence is independent of the polynomial degree of boundary NURBS. However, greater difference between p_B and p_c will lead to more accurate results. The results of NURBS-HCG converge in general to the theoretical convergence rates (p_c). This is also the case with increasing number of boundary control points. The results also converge with the theoretical convergence rates (p_c). Moreover, the rate of convergence is independent of the total number of boundary control points. These observations are therefore valid for the 2D as well as the 3D case. For further details on the effect of p_B and N_B , see also the studies of Chen et al. (2015).

(c) *Efficiency of the NURBS-HCGM*

The efficiency of the NURBS-HCGM is hereafter investigated as it is of fundamental importance and largely determines the potential of the method for the use in engineering applications. Here, for simplicity, we only give a brief discussion about it. For a detailed investigation, the reader can refer to Klinkel et al. (2015). The efficiency of the NURBS-HCGM is mainly determined by the choice of p_B , N_B , p_C , and N_C , see Eq. (48). However, the size of the matrix in Eq. (48) enlarges primarily with the rise of the number of boundary control points N_B and collocation points N_C , which accordingly increases the computation time. Order elevation of the polynomial degrees p_B and p_C plays a minor role for the computation time. Computational costs occur only for the computation of the NURBS basis functions and their derivatives. There is no influence on the dimension of the matrices in Eq. (48). As a result, the total computation time does not change significantly with the rise of p_B and p_C . As already mentioned, however, a specific polynomial degree of boundary NURBS and number of boundary control points should be employed to achieve a high level of accuracy with respect to the exact solution. In addition, it has been already observed that a higher polynomial degree of collocation NURBS and larger number of collocation points should be applied to ensure the accuracy of the NURBS-HCGM. Hence, the optimal choice of p_B , p_C and N_B , N_C is significant for an efficient and accurate computation. To meet this need, we suggest the following two rules for the application of the NURBS-HCGM in the analysis:

1. Initially apply order elevation for the polynomial degree of boundary NURBS p_B . Thereafter, increase the number of boundary control points N_B . These steps ensure the accuracy with respect to the exact solution.
2. Apply order elevation of the polynomial degree of collocation NURBS p_C and increase the number of collocation points N_C in order to achieve high accuracy of the NURBS-HCGM. Note, that order elevation is computationally more efficient than increasing the number of collocation points as discussed above.

(d) *Accuracy in respect to the exact solution*

It has been observed that the convergence behavior of the NURBS-HCGM is equal to the convergence behavior of the eigenvalue method with respect to the analytical solution by Timoshenko (1951). This holds both for low and high polynomial degrees of boundary NURBS (Chen et al. 2015). Order elevation or h -refinement of the boundary NURBS entails more accurate results. The very good agreement between the results of the eigenvalue method and the NURBS-HCGM results certifies also the validity and rationality of the aforementioned rules for the best possible convergence behavior.

Similar results have been observed by comparing the NURBS-G with the eigenvalue method with respect to the analytical solution. According to Chen et al. (2016), the convergence behavior of the NURBS-G is equal to the convergence behavior of the eigenvalue method, both for low and high polynomial degrees of boundary NURBS. Order elevation or h -refinement of the boundary NURBS entails more accurate results as is also the case for the NURBS-HCGM.

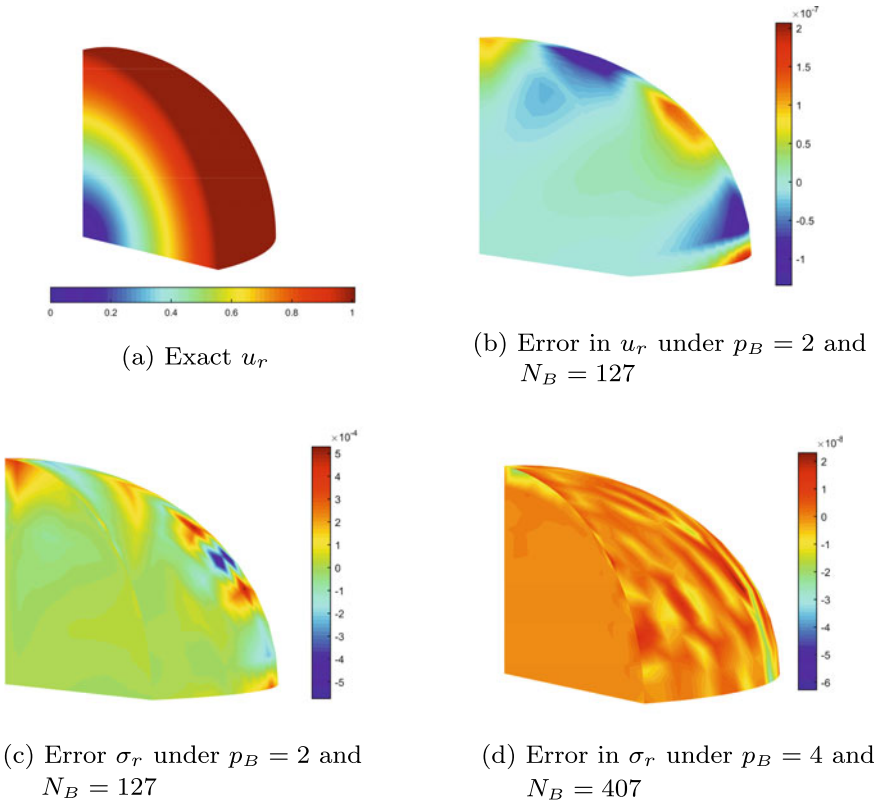


Fig. 19 u_r and σ_r plots of the 3D solid sphere under hydrostatic pressure. Here, for the radial NURBS, the polynomial degree is $p_c = p_b$ and the number of radial control points is $N_c = \text{ceil}(N_B/2) + p_c$

Finally, we will present the contour plot of the analytical solution and the errors in the radial displacement (u_r) and stress (σ_r) at the boundary surfaces ($\xi = 1$) obtained by the NURBS-G. Here, the error is defined as the difference between the numerical solution and the analytical solution. It should be noted that the radial stress σ_r is homogeneous as shown in Eq. (56). Hence, we will only show the error of the radial stress under two different boundary descriptions. The results are shown in Fig. 19. It can be seen in the figures that the error level of the NURBS-G is quite low, which implies that the method performs accurately.

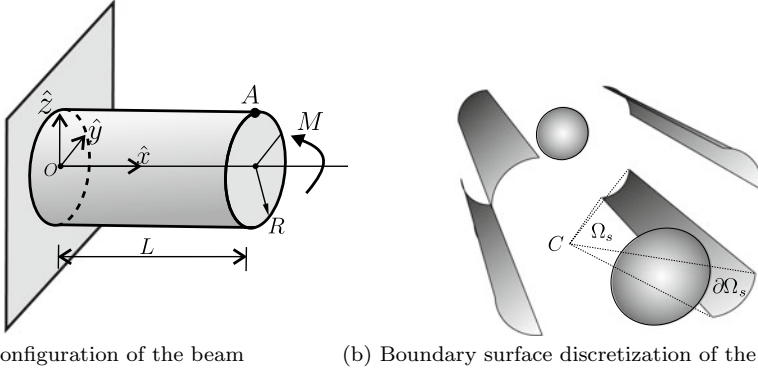


Fig. 20 Cantilever beam subjected to bending moment

5.3 Circular Cantilever Beam Subjected to Bending Moment

The aim of this example is to demonstrate the capability of the NURBS-HCGM. Therefore, the standard FEM and the NURBS-HCGM are compared to the analytical solution for a cantilever beam subjected to bending moment. Further studies of the same system under torsional moment have been carried out by Chen et al. (2015). The configuration of the beam is presented in Fig. 20a. The material properties of the beam are: Young's modulus $E = 100 \text{ N/m}^2$, Poisson's ratio $\nu = 0.0$. The beam has a length of $L = 50 \text{ m}$ and radius of $R = 5 \text{ m}$. The external bending moment is $M = 1000 \text{ N} \cdot \text{m}$. The scaling center C is defined as the center of the beam, $(\hat{x}_0, \hat{y}_0, \hat{z}_0) = (25 \text{ m}, 0, 0)$. Thus, with respect to the scaling center the domain Ω is partitioned into 6 sections Ω_s bounded by the boundary surfaces $\partial\Omega_s$, see Fig. 20b. An analytical solution is given by Timoshenko (1951) and is considered here as the reference solution. The vertical displacement w (\hat{z} -direction) of the cantilever beam subjected to the tip bending moment M is given by

$$w = \frac{M}{2EI} (\hat{x}^2 + \nu \hat{y}^2 - \nu \hat{z}^2). \quad (57)$$

The standard FEM and the NURBS-HCGM are employed to solve the problem. The boundary surface of each section Ω_s is initially described by NURBS basis functions with polynomial degree $p_B = 2$ and the open knot vector $\mathbf{H} = \mathbf{Z} = [0, 0, 0, 0.5, 1, 1, 1]$. The polynomial degree is elevated to $p_B = 3$ and 4. For each polynomial degree of boundary NURBS, the number of elements per parametric direction is initially $n = 2$, and is increased to $n = 3, 4, 5$, and 6 using h -refinement. The control polygon and the element mesh of the boundary surfaces of the beam are presented in Fig. 21. The contour plot of the displacement is presented in Fig. 22. Note that the contour is very smooth. The L^∞ -norm for the error of the displacement at point A (Fig. 20a, $\mathbf{x}_A = (50 \text{ m}, 0, 5 \text{ m})$) is employed to demonstrate the accuracy

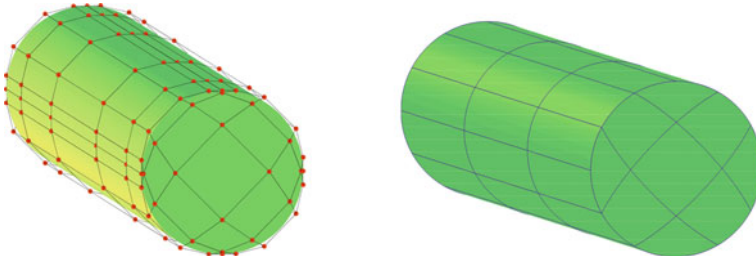
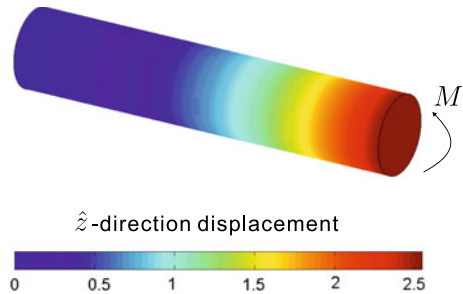


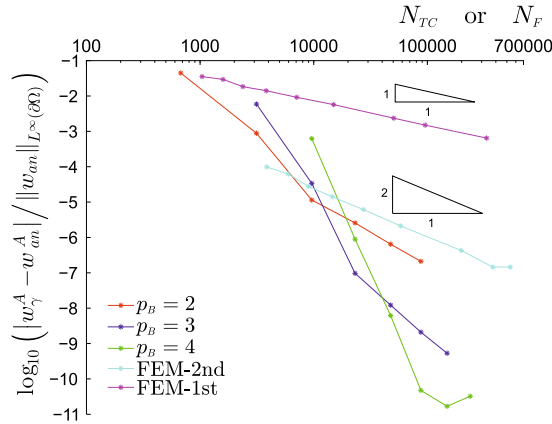
Fig. 21 Control polygon and mesh on the boundary surfaces of the beam ($p_B = 3$ and 3 elements per parametric direction)

Fig. 22 Displacement contour ($p_B = 3$ and 3 elements per parametric direction)



of both methods, see Fig. 23. In the figure, w_γ^A denotes the deformation obtained from the numerical solution, which is either NURBS-HCGM or standard FEM. For the NURBS-HCGM, the rules proposed in the previous example are employed. The polynomial degree of collocation NURBS is defined as $p_c = \text{even}(p_B + 6)$. The number of collocation points is determined as $N_c = N_B$. The standard FEM employs full Gauss quadrature (Hughes 2000). Both linear and quadratic shape functions are used and are denoted as FEM-1st and FEM-2nd, see Fig. 23. Here, the error norm is plotted versus the total number of collocation points for NURBS-HCGM given by $N_{TC} = N_c \times N_B$, and versus the total number of nodes employed in the standard FEM, which is denoted by N_F .

Figure 23 shows that the NURBS-HCGM yields accurate results on the basis of the proposed rules. It approaches the analytical solution with increasing polynomial degree of the boundary NURBS and with increasing total number of collocation points. The NURBS-HCGM and the standard FEM yield error levels in the same range with respect to the total number of collocation points or FEM-nodes, respectively. In case of a coarse discretization the standard FEM performs better than the NURBS-HCGM, for finer discretizations the NURBS-HCGM outperforms the standard FEM.



Vertical displacement at point A under bending moment

Fig. 23 Relative error of the displacement at point A. Here, w_γ^A and w_γ^{AR} denote the deformations obtained from the numerical solution, which is either NURBS-HCGM or the standard FEM

5.4 Hollow Circular Cylinder Subjected to Internal Pressure

The aim of this numerical example is to investigate the capability of the NURBS-HCGM. Therefore, the standard IGA and the NURBS-HCGM are compared with the analytical solution for a hollow circular cylinder subjected to internal pressure. The geometry of the cylinder is shown in Fig. 24. Plane strain conditions are assumed in the axial direction. A constant pressure is applied at the inner surface of the cylinder. Here, the inner and outer radius are $R_a = 1$ m, and $R_b = 2$ m, respectively. The properties of the cylinder are defined by a Young’s modulus $E = 40$ N/m² and a Poisson’s ratio $\nu = 0.0$. The magnitude of the inner pressure is $p = 20$ N/m². Considering symmetry only a quarter of the cylinder is modeled, see Fig. 24b. The scaling center C is defined as the average coordinate of all control points at the boundary. With respect to the scaling center, the domain Ω is partitioned into 6 sections Ω_s bounded by the boundary surfaces $\partial\Omega_s$, see Fig. 24c.

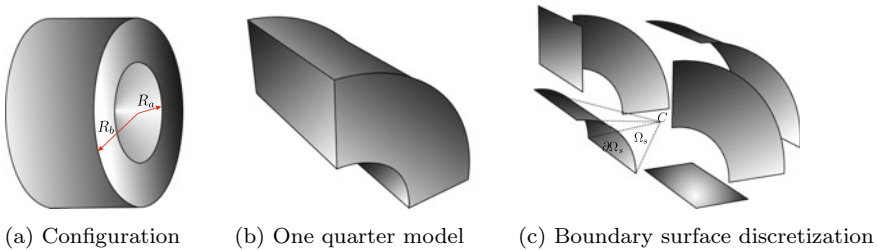


Fig. 24 Thick cylinder subjected to internal pressure

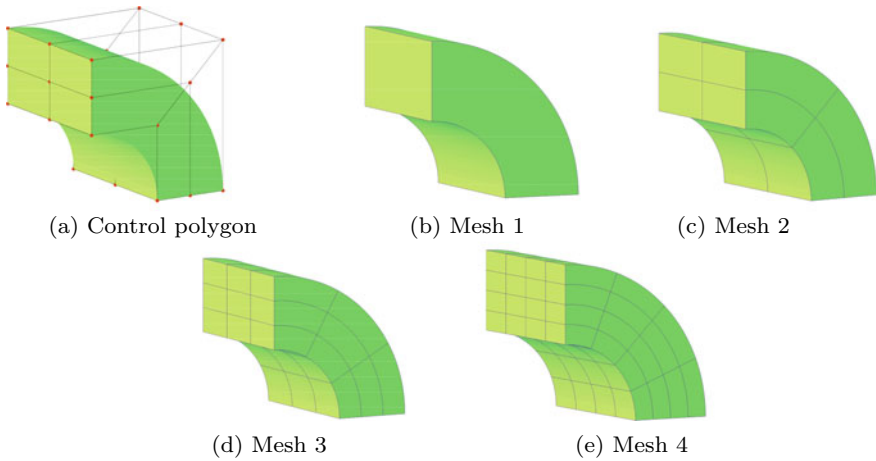


Fig. 25 Control polygon (1 element per parametric direction) and mesh on the boundary surfaces of the quarter cylinder ($p_B = 2$)

An analytical solution for the displacement response is given by Hughes et al. (2005). A plot of the control polygon is presented in Fig. 25a. Element meshes attained by h -refinement are shown in Fig. 25b–e. The polynomial degree is $p_B = 2$ in all cases. The initial open knot vector is $\mathbf{H} = \mathbf{Z} = [0, 0, 0, 1, 1, 1]$. The rules proposed in the previous examples are employed for the NURBS-HCGM. The polynomial degree of the collocation NURBS is defined as $p_C = \text{even}(p_B + 6)$, and the number of collocation points is determined by $N_C = N_B$.

Results of the displacement solution for each mesh are presented in Fig. 26. The contour plot of the radial displacement of the cylinder given in Fig. 26a is clearly apparent. Errors in the radial displacement are plotted in Fig. 26b. For better illustration, the result taken from Hughes et al. (2005) for Mesh 1 is also presented in the figure. Hughes et al. (2005) employed the isogeometric approach for the analysis. The maximum error of this approach is slightly below that of the proposed method (Mesh 1). The maximum error through the cylinder thickness attained with the NURBS-HCGM is: for Mesh 1 approximately 1.5%, for Mesh 2 approximately 0.25%, for Mesh 3 0.08%, and for Mesh 4 0.01%. Higher accuracy of the displacement solution can be achieved on all meshes by increasing the polynomial degree p_B for the boundary NURBS.

5.5 Solid with Free Form Geometry and Arbitrary Number of Boundary Surfaces

The last numerical example is employed to illustrate the capability of the NURBS-G to deal with 3D solids bounded by an arbitrary number of boundary surfaces.

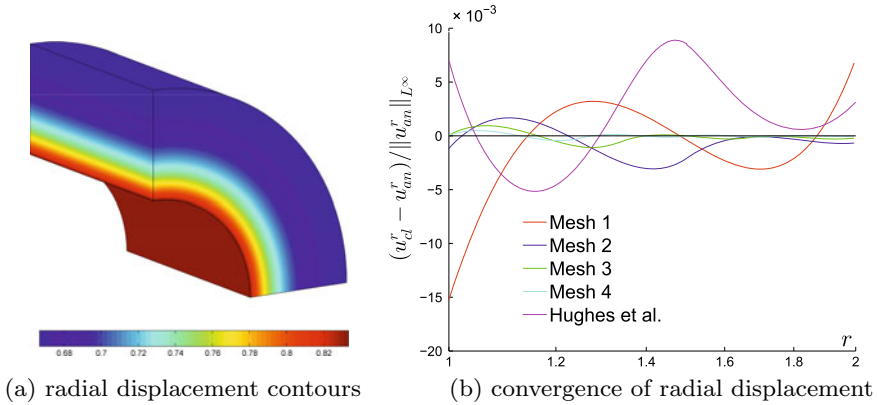


Fig. 26 Radial displacement of the quarter cylinder. Here, u_{cl}^r denotes the displacements either computed with the NURBS-HCGM or taken from Hughes et al. (2005). u_{an}^r represents the displacements obtained from the analytical solution

Therefore, the standard FEM and the NURBS-G are compared for a solid loaded by surface tractions. The system is depicted in Fig. 27a, b. The material properties of the solid are defined by Young's modulus $E = 100 \text{ N/m}^2$ and Poisson's ratio $\nu = 0.0$. The initial geometry of the boundary surface is described by NURBS basis functions of polynomial degree $p_b = 2$ and open knot vectors $\mathbf{H} = \mathbf{Z} = [0, 0, 0, 1, 1, 1]$. For the response analysis, order elevation and h -refinement are performed to generate boundary NURBS with higher polynomial degree and a larger number of elements. For the NURBS-G, the polynomial degree of radial NURBS is defined as $p_c = p_b$. The number of radial control points is set as $N_c = \text{ceil}(N_b/4) + p_c$. In the NURBS-G, the reduced quadrature with $\text{ceil}(p_c/2)+1$ Gauss points per element is employed to perform the integration in Eq. (53).

The geometry of elastic cube with circular hole is defined by the length of cube $B = L = H = 40 \text{ m}$ and the radius of circular hole $R = 10 \text{ m}$. The magnitude of surface traction is $p = 10 \text{ N/m}^2$. Due to the symmetry of the problem, only one-eighth of the cube is considered with the symmetric boundary conditions, see Fig. 27b. In the analysis, the scaling center C is defined as the center of the one-eighth cube. With respect to the center, the domain Ω is partitioned into 7 sections Ω_s bounded by the boundary surfaces $\partial\Omega_s$, see Fig. 27c.

Sample plots of control polygon and mesh on the boundary surfaces of the one-eighth cube are presented in Fig. 28. An analytical solution for this problem in terms of displacements is not available. Thus, the comparison is made between the standard FEM and the NURBS-G. In the standard FEM, quadratic shape function (C3D20) and full Gauss quadrature integration are employed (Hughes et al. 2010). The computation is performed in Abaqus (2007) with 55273 elements and 235171 nodes. The contour plots of the vertical displacement for both methods are presented in Fig. 29. As it can be seen in the figure, good agreement is achieved.

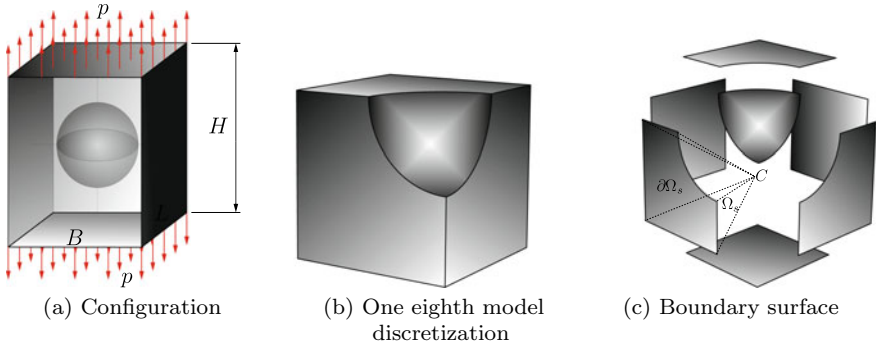


Fig. 27 Elastic cube with circular hole in tension regime

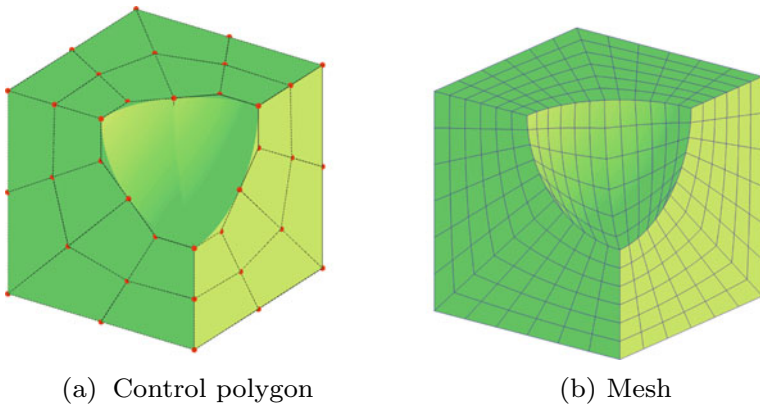


Fig. 28 Control polygon ($p_B = 2$ and 1 element per parametric direction) and mesh ($p_B = 6$ and 6 elements per parametric direction) on the boundary surfaces of the one-eighth cube

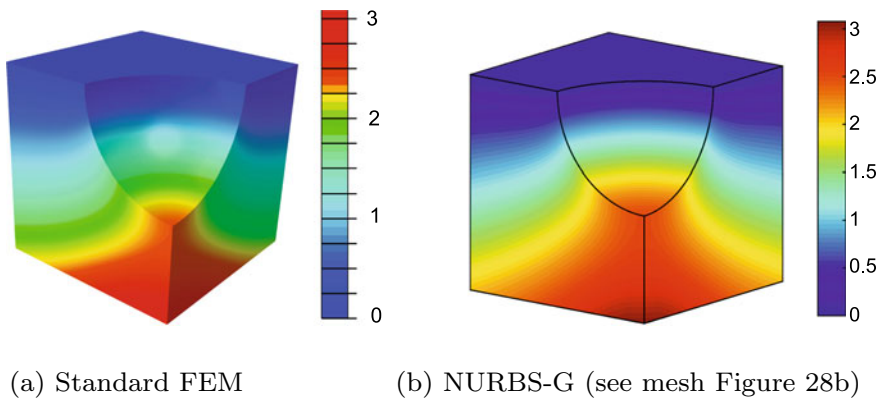


Fig. 29 Contours of the vertical displacement for the one-eighth cube

6 Summary

We have discussed in this chapter numerical approaches to analyze solids in an isogeometric framework. These analysis procedures are well suited for structures designed by the boundary representation modeling technique. This is a popular technique to define solids in CAD. In the analysis, the solid is represented by its boundary and a radial scaling center. Employing the boundary scaling technique of the SB-FEM, the solid can be generated by scaling the boundary with respect to the scaling center. Here, the boundary geometry and the displacement response are modeled by the NURBS basis functions, which are the same functions used for the definition of the geometry. For the approximation of the displacement response in the interior domain the eigenvalue method can be employed for linear problems. Alternatively, one-dimensional NURBS basis function is introduced in combination with a collocation scheme in the scaling direction for the approximation of the displacement response. The NURBS approximation in scaling direction enables also the treatment of nonlinear problems. Finally, the weak form of equilibrium can be enforced separately in the circumferential direction and also in the scaling direction in the scope of a purely Galerkin approach. Moreover, we have presented numerical examples to illustrate the efficiency and accuracy of the approaches. After observing the results, we have provided suggestions for the optimal choice of polynomial degree of collocation NURBS and collocation points in scaling direction. It is worth remarking that compared with the NURBS-based collocation, there is no singularity arising at the scaling center in a Galerkin context. Hence, the solution procedure is stable. In addition, the error level of a Galerkin approach is lower than that of the NURBS-based collocation and higher rate of convergence is achieved. Furthermore, we have seen that the rate of convergence for both approaches is primarily dependent on the NURBS description in the scaling direction and it is independent of the boundary description. In regard to practical applications, we have demonstrated comparisons of the boundary-oriented approaches with analytical solution, the standard FEM and isogeometric analysis (IGA). A good agreement is achieved in all cases. To sum up, we consider the presented boundary-oriented formulations as promising analysis frameworks that can be extended to a wide class of problems including nonlinearities and complex geometries such as trimmed NURBS.

Appendix

The normal vectors \mathbf{n}^ξ , \mathbf{n}^η and \mathbf{n}^ζ are perpendicular to the surface described by the parameters (η, ζ) , (ζ, ξ) and (ξ, η) , respectively, see Fig. 3. They are summarized as

$$\begin{aligned} \mathbf{n}^\xi &= [n_{\hat{x}}^\xi, n_{\hat{y}}^\xi, n_{\hat{z}}^\xi]^T = \frac{\hat{\mathbf{x}}_{s,\eta} \times \hat{\mathbf{x}}_{s,\zeta}}{\|\hat{\mathbf{x}}_{s,\eta} \times \hat{\mathbf{x}}_{s,\zeta}\|} = \frac{\mathbf{x}_{s,\eta} \times \mathbf{x}_{s,\zeta}}{\|\mathbf{x}_{s,\eta} \times \mathbf{x}_{s,\zeta}\|} \\ &= \frac{1}{g^\xi} \begin{bmatrix} y_{s,\eta} z_{s,\zeta} - z_{s,\eta} y_{s,\zeta} \\ z_{s,\eta} x_{s,\zeta} - x_{s,\eta} z_{s,\zeta} \\ x_{s,\eta} y_{s,\zeta} - y_{s,\eta} x_{s,\zeta} \end{bmatrix}, \end{aligned} \quad (\text{A.1})$$

$$\begin{aligned} \mathbf{n}^\eta &= [n_{\hat{x}}^\eta, n_{\hat{y}}^\eta, n_{\hat{z}}^\eta]^T = \frac{\hat{\mathbf{x}}_{s,\zeta} \times \hat{\mathbf{x}}_{s,\xi}}{\|\hat{\mathbf{x}}_{s,\zeta} \times \hat{\mathbf{x}}_{s,\xi}\|} = \frac{\mathbf{x}_{s,\zeta} \times (\mathbf{x}_s - \hat{\mathbf{x}}_0)}{\|\mathbf{x}_{s,\zeta} \times (\mathbf{x}_s - \hat{\mathbf{x}}_0)\|} \\ &= \frac{1}{g^\eta} \begin{bmatrix} (z_s - \hat{z}_0)y_{s,\zeta} - (y_s - \hat{y}_0)z_{s,\zeta} \\ (x_s - \hat{x}_0)z_{s,\zeta} - (z_s - \hat{z}_0)x_{s,\zeta} \\ (y_s - \hat{y}_0)x_{s,\zeta} - (x_s - \hat{x}_0)y_{s,\zeta} \end{bmatrix}, \end{aligned} \quad (\text{A.2})$$

$$\begin{aligned} \mathbf{n}^\zeta &= [n_{\hat{x}}^\zeta, n_{\hat{y}}^\zeta, n_{\hat{z}}^\zeta]^T = \frac{\hat{\mathbf{x}}_{s,\xi} \times \hat{\mathbf{x}}_{s,\eta}}{\|\hat{\mathbf{x}}_{s,\xi} \times \hat{\mathbf{x}}_{s,\eta}\|} = \frac{(\mathbf{x}_s - \hat{\mathbf{x}}_0) \times \mathbf{x}_{s,\eta}}{\|(\mathbf{x}_s - \hat{\mathbf{x}}_0) \times \mathbf{x}_{s,\eta}\|} \\ &= \frac{1}{g^\zeta} \begin{bmatrix} (y_s - \hat{y}_0)z_{s,\eta} - (z_s - \hat{z}_0)y_{s,\eta} \\ (z_s - \hat{z}_0)x_{s,\eta} - (x_s - \hat{x}_0)z_{s,\eta} \\ (x_s - \hat{x}_0)y_{s,\eta} - (y_s - \hat{y}_0)x_{s,\eta} \end{bmatrix} \end{aligned} \quad (\text{A.3})$$

where g^ξ , g^η and g^ζ are considered according to Chen et al. (2015, 2016). The transformation of an infinitesimal surface element dS is derived by employing Eqs. (1) and (A.1)–(A.3) as

$$dS^\xi = |\hat{\mathbf{x}}_{s,\eta} \times \hat{\mathbf{x}}_{s,\zeta}| d\eta d\zeta = |\xi \mathbf{x}_{s,\eta} \times \xi \mathbf{x}_{s,\zeta}| d\eta d\zeta = \xi^2 g^\xi d\eta d\zeta, \quad (\text{A.4})$$

$$dS^\eta = |\hat{\mathbf{x}}_{s,\zeta} \times \hat{\mathbf{x}}_{s,\xi}| d\zeta d\xi = |\xi \mathbf{x}_{s,\zeta} \times (\mathbf{x}_s - \hat{\mathbf{x}}_0)| d\zeta d\xi = \xi g^\eta d\zeta d\xi, \quad (\text{A.5})$$

$$dS^\zeta = |\hat{\mathbf{x}}_{s,\xi} \times \hat{\mathbf{x}}_{s,\eta}| d\xi d\eta = |(\mathbf{x}_s - \hat{\mathbf{x}}_0) \times \xi \mathbf{x}_{s,\eta}| d\xi d\eta = \xi g^\zeta d\xi d\eta. \quad (\text{A.6})$$

References

- Abaqus. (2001). *6.7. User's manual*. Dassault Systemes.
- Apostolatos, A., Schmidt, R., Wüchner, R., & Bletzinger, K. U. (2014). A Nitsche-type formulation and comparison of the most common domain decomposition methods in isogeometric analysis. *International Journal for Numerical Methods in Engineering*, 97(7), 473–504.
- Auricchio, F., da Veiga, L. B., Hughes, T. J. R., Reali, A., & Sangalli, G. (2010). Isogeometric collocation methods. *Mathematical Models and Methods in Applied Sciences*, 20(11), 2075–2107.
- Auricchio, F., da Veiga, L. B., Hughes, T. J. R., Reali, A., & Sangalli, G. (2012). Isogeometric collocation for elastostatics and explicit dynamics. *Computer Methods in Applied Mechanics and Engineering*, 249, 2–14.
- Bazilevs, Y., Long, C. C., Akkerman, I., Benson, D. J., & Shashkov, M. J. (2014). Isogeometric analysis of lagrangian hydrodynamics: Axisymmetric formulation in the rz-cylindrical coordinates. *Journal of Computational Physics*, 262, 244–261.
- Behnke, R., Mundil, M., Birk, C., & Kaliske, M. (2014). A physically and geometrically nonlinear scaled-boundary-based finite element formulation for fracture in elastomers. *International Journal for Numerical Methods in Engineering*, 99, 966–999.

- Breitenberger, M., Apostolatos, A., Philipp, B., Wüchner, R., & Bletzinger, K. U. (2015). Analysis in computer aided design: Nonlinear isogeometric B-Rep analysis of shell structures. *Computer Methods in Applied Mechanics and Engineering*, 284, 401–457.
- Chasapi, M., & Klinkel, S. (2018). A scaled boundary isogeometric formulation for the elasto-plastic analysis of solids in boundary representation. *Computer Methods in Applied Mechanics and Engineering*, 333, 475–496.
- Chen, L., Dornisch, W., & Klinkel, S. (2015). Hybrid collocation-Galerkin approach for the analysis of surface represented 3D-solids employing SB-FEM. *Computer Methods in Applied Mechanics and Engineering*, 295, 268–289.
- Chen, L., Simeon, B., & Klinkel, S. (2016). A NURBS based Galerkin approach for the analysis of solids in boundary representation. *Computer Methods in Applied Mechanics and Engineering*, 305, 777–805.
- Cottrell, J. A., Hughes, T. J. R., & Bazilevs, Y. (2009). *Isogeometric analysis: Toward integration of CAD and FEA*. John Wiley & Sons.
- De Lorenzis, L., Evans, J. A., Hughes, T. J. R., & Reali, A. (2015). Isogeometric collocation: Neumann boundary conditions and contact. *Computer Methods in Applied Mechanics and Engineering*, 282, 21–54.
- Dornisch, W., Klinkel, S., & Simeon, B. (2013). Isogeometric Reissner-Mindlin shell analysis with exactly calculated director vectors. *Computer Methods in Applied Mechanics and Engineering*, 253, 491–504.
- Dornisch, W., Vitucci, G., & Klinkel, S. (2015). The weak substitution method - an application of the mortar method for patch coupling in NURBS-based isogeometric analysis. *International Journal for Numerical Methods in Engineering*, 103, 205–234.
- Düster, A., Parvizian, J., Yang, Z., & Rank, E. (2008). The finite cell method for three-dimensional problems of solid mechanics. *Computer Methods in Applied Mechanics and Engineering*, 197(45), 3768–3782.
- Gomez, H., & De Lorenzis, L. (2016). The variational collocation method. *Computer Methods in Applied Mechanics and Engineering*, 309, 152–181.
- Hughes, T. J. R. (2000). *The finite element method: Linear static and dynamic finite element analysis*. Courier Dover Publications.
- Hughes, T. J. R., Cottrell, J. A., & Bazilevs, Y. (2005). Isogeometric analysis: CAD, finite elements, NURBS, exact geometry and mesh refinement. *Computer Methods in Applied Mechanics and Engineering*, 194, 4135–4195.
- Hughes, T. J. R., Reali, A., & Sangalli, G. (2010). Efficient quadrature for NURBS-based isogeometric analysis: Computational Geometry and Analysis. *Computer Methods in Applied Mechanics and Engineering*, 199, 301–313.
- Kiendl, J., Auricchio, F., da Veiga, L. B., Lovadina, C., & Reali, A. (2015). Isogeometric collocation methods for the Reissner-Mindlin plate problem. *Computer Methods in Applied Mechanics and Engineering*, 284, 489–507.
- Klinkel, S., Chen, L., & Dornisch, W. (2015). A NURBS based hybrid collocation-Galerkin method for the analysis of boundary represented solids. *Computer Methods in Applied Mechanics and Engineering*, 284, 689–711.
- Lin, G., Zhang, Y., Hu, Z., & Zhong, H. (2014). Scaled boundary isogeometric analysis for 2D elastostatics. *Science China Physics, Mechanics and Astronomy*, 57(3), 286–300.
- Lin, Z., & Liao, S. (2011). The scaled boundary FEM for nonlinear problems. *Communications in Nonlinear Science and Numerical Simulation*, 16(1), 63–75.
- Natarajan, S., Wang, J. C., Song, C., & Birk, C. (2015). Isogeometric analysis enhanced by the scaled boundary finite element method. *Computer Methods in Applied Mechanics and Engineering*, 283, 733–762.
- Ooi, E., Song, C., & Tin-Loi, F. (2014). A scaled boundary polygon formulation for elasto-plastic analyses. *Computer Methods in Applied Mechanics and Engineering*, 268, 905–937.
- Piegl, L. & Tiller, W. (1997). *The NURBS book*. Monographs in visual communications. Springer.

- Rank, E., Ruess, M., Kollmannsberger, S., Schillinger, D., & Düster, A. (2012). Geometric modeling, isogeometric analysis and the finite cell method. *Computer Methods in Applied Mechanics and Engineering*, 249, 104–115.
- Reali, A., & Gomez, H. (2015). An isogeometric collocation approach for Bernoulli-Euler beams and Kirchhoff plates. *Computer Methods in Applied Mechanics and Engineering*, 284, 623–636.
- Ruess, M., Schillinger, D., Özcan, A. I., & Rank, E. (2014). Weak coupling for isogeometric analysis of non-matching and trimmed multi-patch geometries. *Computer Methods in Applied Mechanics and Engineering*, 269, 46–71.
- Schillinger, D., Evans, J. A., Reali, A., Scott, M. A., & Hughes, T. J. R. (2013). Isogeometric collocation: Cost comparison with Galerkin methods and extension to adaptive hierarchical NURBS discretizations. *Computer Methods in Applied Mechanics and Engineering*, 267, 170–232.
- Schmidt, R., Wüchner, R., & Bletzinger, K. U. (2012). Isogeometric analysis of trimmed NURBS geometries. *Computer Methods in Applied Mechanics and Engineering*, 241–244, 93–111.
- Song, C. (2004). A matrix function solution for the scaled boundary finite-element equation in statics. *Computer Methods in Applied Mechanics and Engineering*, 193(23), 2325–2356.
- Song, C., & Wolf, J. P. (1997). The scaled boundary finite-element method—alias consistent infinitesimal finite-element cell method—for elastodynamics. *Computer Methods in Applied Mechanics and Engineering*, 147, 329–355.
- Song, C., & Wolf, J. P. (1998). The scaled boundary finite-element method: analytical solution in frequency domain. *Computer Methods in Applied Mechanics and Engineering*, 164(1–2), 249–264.
- Stroud, I. (2006). *Boundary representation modelling techniques*. Springer.
- Temizer, I., Wriggers, P., & Hughes, T. J. R. (2012). Three-dimensional mortar-based frictional contact treatment in isogeometric analysis with NURBS. *Computer Methods in Applied Mechanics and Engineering*, 209, 115–128.
- Timoshenko, S. (1951). *Theory of elasticity*. Engineering societies monographs: McGraw-Hill.